CHAPTER 5: FIELD TEST RESULTS

Results and discussions of the field investigation are presented in this chapter. The following field investigations were carried out. (See also Chapter 3):

- Nondestructive assessment and residual flexural strength testing on salvaged box beams from a highway bridge in Kent County
- Nondestructive assessment of segments of segmental bridge carrying US-131 over Muskegon River. (Southbound lanes, 6 miles South of Big Rapids)
- Nondestructive assessment of segments of bridge S08-(box beams 3-M-11 and 3-A-8) of I-96 over Canal Road, Dimondale, near Lansing.

5.1 Salvaged Box Beams from Kent County

Nondestructive assessment and residual flexural testing of three side-by-side salvaged box beams decommissioned by Kent County Road Commission after 39 years of service due to deterioration were conducted at LTU laboratories. The study assessed how the observed deterioration in both concrete quality and prestressed strands had affected the overall flexural capacity of these beams. Each beam was 43'-8" long, 36" wide and 21" deep. The three box beams were selected from different parts of the bridge and were representative of the varied levels of environmental exposure. The selection of the three beams was done in agreement with representative of the MDOT Technical Advisory Team.

5.1.1 Ultrasonic Assessment of Salvaged Box Beams.

Results of ultrasonic assessment of the bottom strands of salvaged box beams are presented in this section. The objective was to verify the efficacy of ultrasonic assessment using a 3D ultrasonic tomographer to assess hidden delamination which are usually associated with corroded strands. A comparative study was conducted where the intensity of the reflected signals measured along areas with expected corroded strands have been compared to those along areas with less corroded strands to infer the degree of concrete damage and gaps created by corrosion product around these strands. Expected corroded strands were located in areas with visual confirmation of rust stains and cracking. Recalling the basic principle behind ultrasonic testing, using 3D ultrasonic tomography (MIRA), the intensity of reflections are related to magnitude of change in material properties such

as density and elastic modulus as waves propagate through concrete specimen. It is expected that as strands with advanced corrosion tends to have detectable voids around them due to the fact that the product of corrosion tends to occupy larger volume compared to un-corroded strands. Hence, scans on corroded strands are expected to produce higher reflected intensities compared to scans on un-corroded strands. This is due to the fact that although products of corrosion occupy larger volumes, they have lower densities compared to un-corroded strands and the surrounding concrete. Furthermore, the corrosion products also introduces local debonding between the steel reinforcement and concrete.

A side-by-side comparison of scans at 34.8 decibel (dB) have been compared for different frequencies of 100, 90, 80 and 70 kHz at selected locations along the box beams. The research assistants conducting the testing on the bottom surface of the beams and this activity is shown in Figures 5.1 a and b. The default frequency of shear waves recommended for ultrasonic testing using 3D ultrasonic tomographer is 50 kHz for normal testing. However, for detecting features close to the surface, a higher frequency between the ranges of 70-100 kHz is used and it will emphasize smaller defects. For detecting features at 4 inches (100 mm) depth or more, a lower frequency is preferred. The scan locations were selected based on visual inspection and using results from the Impact Schmidt Hammer to detect locations with lower reflective energy (and difference in sounding indicating hidden delamination). It can be deduced from Figures 5.2 (a) (c) and (e) compared to (b) (d) and (f) at the different frequencies that scans along corroded strands have higher reflected intensities compared to those along less corroded strands. Another observation worth mentioning is that intensity of the reflected scans tends to increase as scanned frequencies increases irrespective of scans along corroded or less corroded strands. This is likely due to the fact that higher scan frequencies tends to have lower wave lengths which tends to pick smaller features compared to lower scanned frequencies. At the same time, higher scan frequencies tends to have higher attenuation tendencies and therefore also unable to detect details at far from the incident surface. Differences in reflected intensities are clearly evident when comparing reflected intensities at the same locations at different densities from Figures 5.2 (a), (c) and (e) from a corroded strand location as against Figures 5.2 (b), (d) and (f) from an un-corroded strand location. Furthermore, if the delamination is initiated (creating an interface) the flange depth is not

detected from the scan results. Figure 5.1 (c) and (d) show strand in corroded state and a strand in less corroded state respectively.

(a) Scan on corroded strand.

(b) Scan on less corrode strand

(c) Corroded strand

(d) Less corroded strand

Figure 5.1 Typical scans on corroded and less corroded strand locations

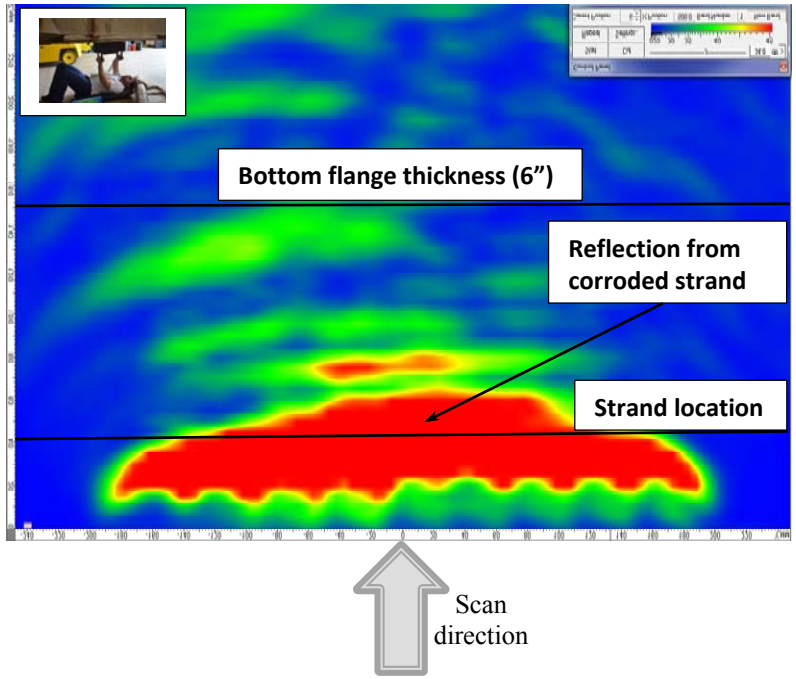

(a) Scan on corroded strand #9 (Beam J11)

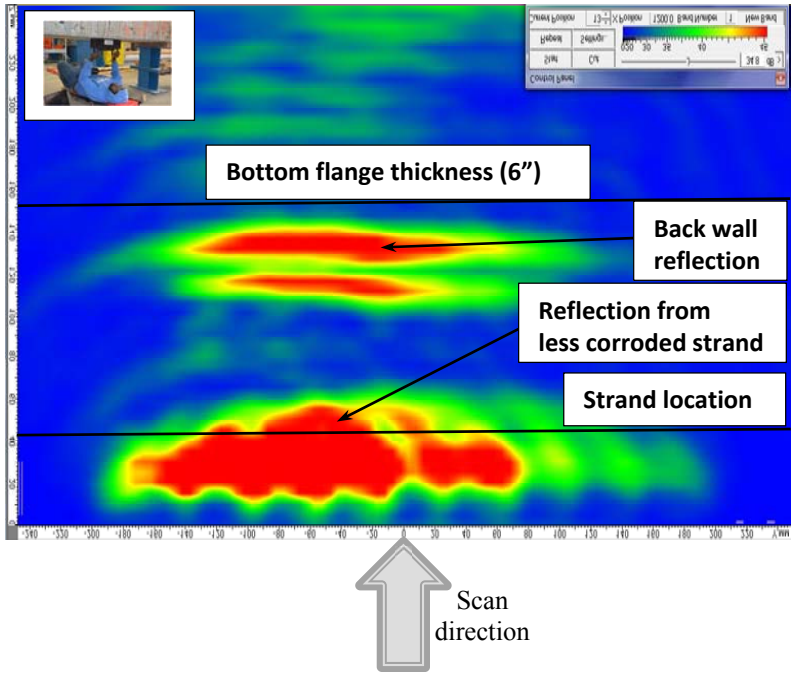

(b) Scan on less corrode strand #7 (Beam H6)

Figure 5.2 Typical scans at 100 kHz, 34.8 dB with (a) along web and (b) at cell location.

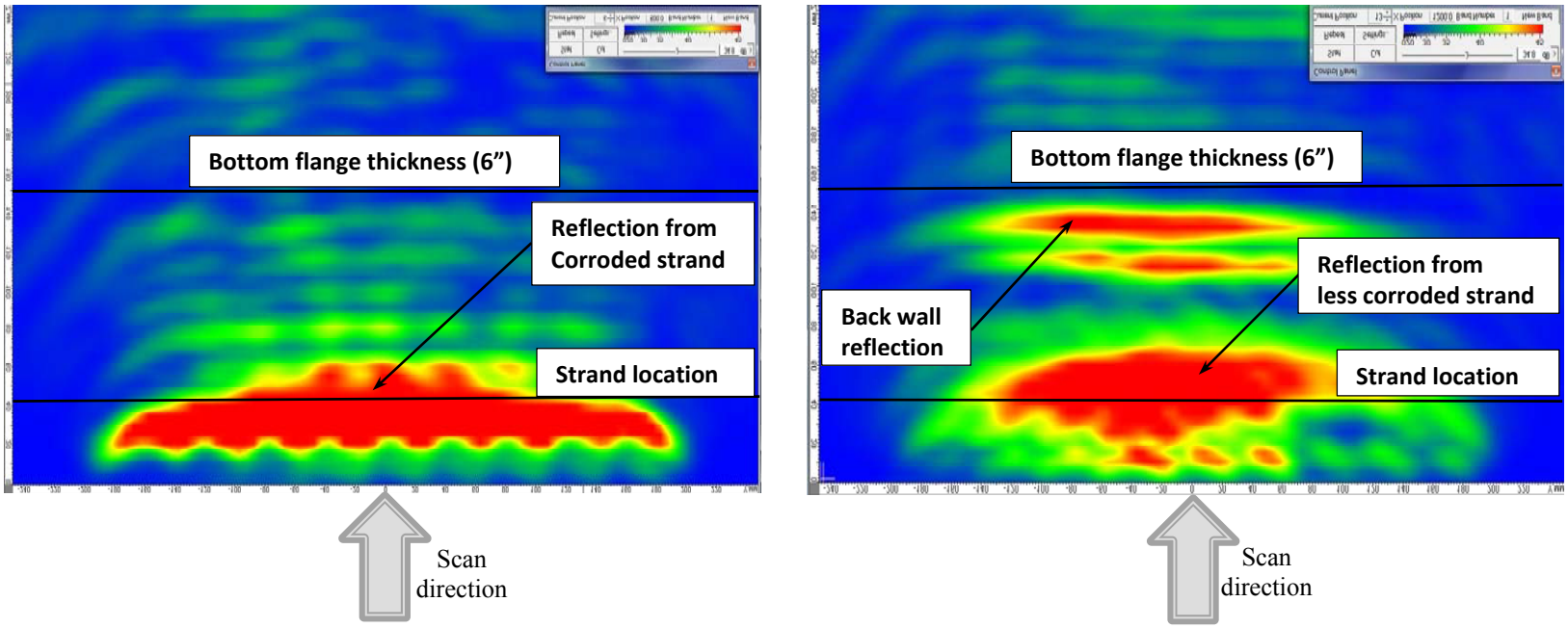

(a) Scan on corroded strand #9 (Beam J11) *(b) Scan on less corrode strand #7 (Beam H6)*

Figure 5.3 Typical scans at 90 kHz, 34.8 dB with (a) along web and (b) at cell location.

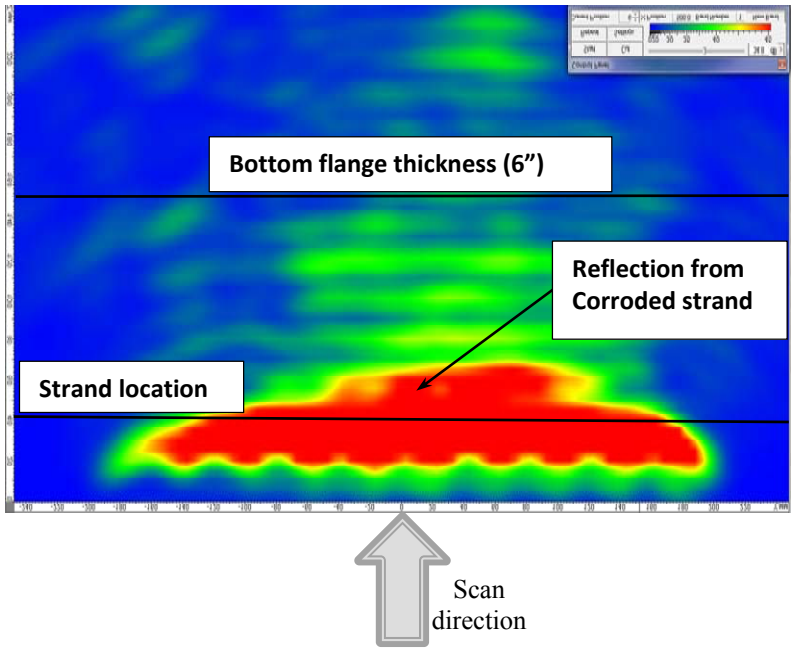

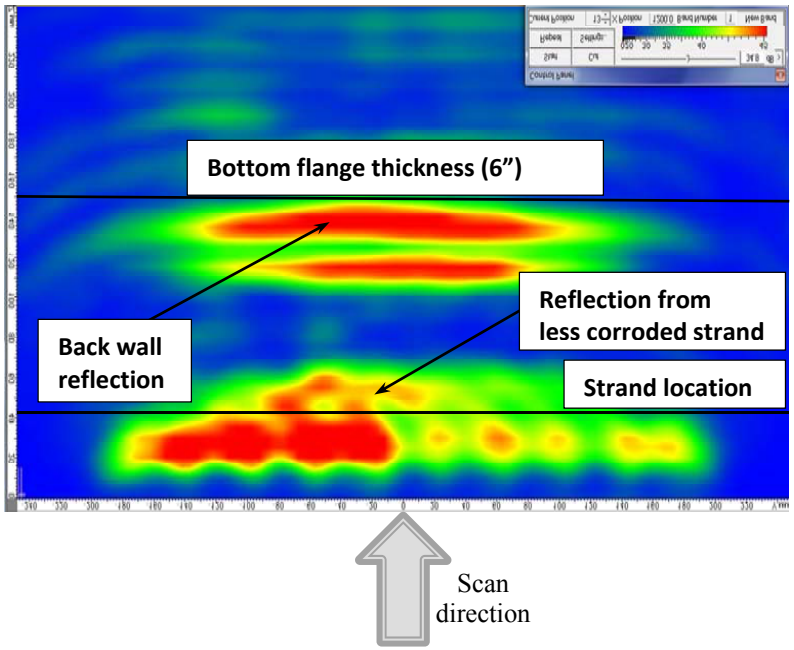

(a) Scan on corroded strand #9 (Beam J11). *(b) Scan on less corrode strand #7 (Beam H6)*

Figure 5.4 Typical scans at 80 kHz, 34.8 dB with (a) along web and (b) at cell location.

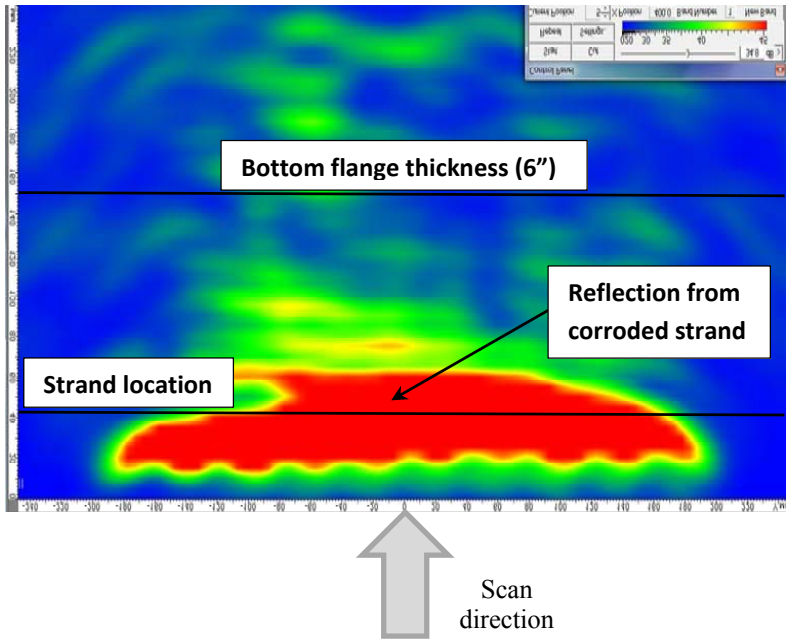

(a) Scan on corroded strand #9 (Beam J11).

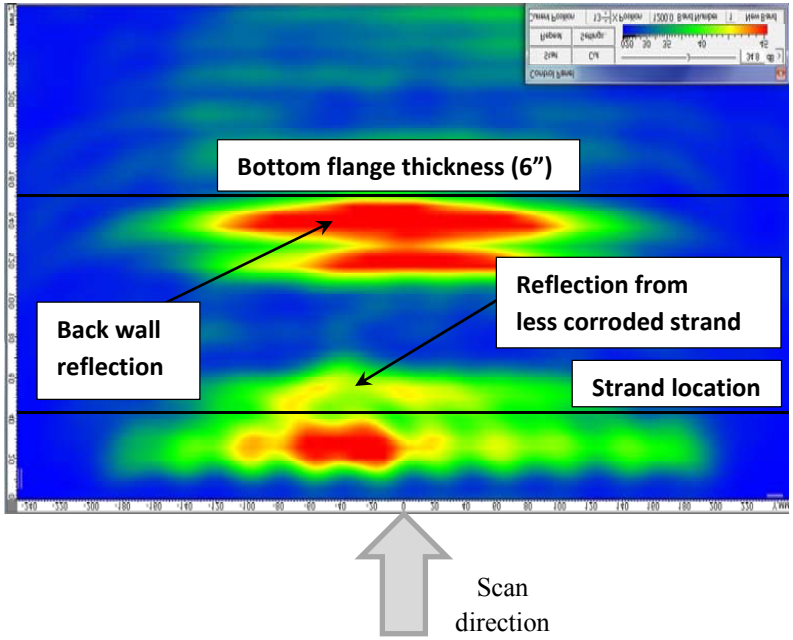

(b) Scan on less corrode strand #7 (Beam H6)

Figure 5.5 Typical scans at 70 kHz, 34.8 dB with (a) along web and (b) at cell location.

Ultrasonic assessment was also used to estimate the side webs and the bottom flange thickness to ascertain if the construction of these box beams conformed to the construction drawings. This was very important as it was part of the scope of this investigation to evaluate the residual flexural strength of these box beams. As part of the investigations, numerical calculations were undertaken to predict the residual failure loads of these salvaged beams at which point the approximate thicknesses of the side webs as well as that of the bottom and top flanges were needed. Details of these calculations can be found in Appendix C of this report. Results of residual flexural tests have been presented in a later section of this chapter. Figure 5.6 show a typical ultrasonic assessment from the side of box beam J11 to estimate the thickness of the web. It can be inferred from Figures 5.7 (a) and (b) that side webs had a thickness of 6 inches (150 mm). Similar assessments were conducted for box beams H6 and A1 to evaluate the side thicknesses.

Figure 5.6: Typical scan on the side of Salvaged Box Beam J11

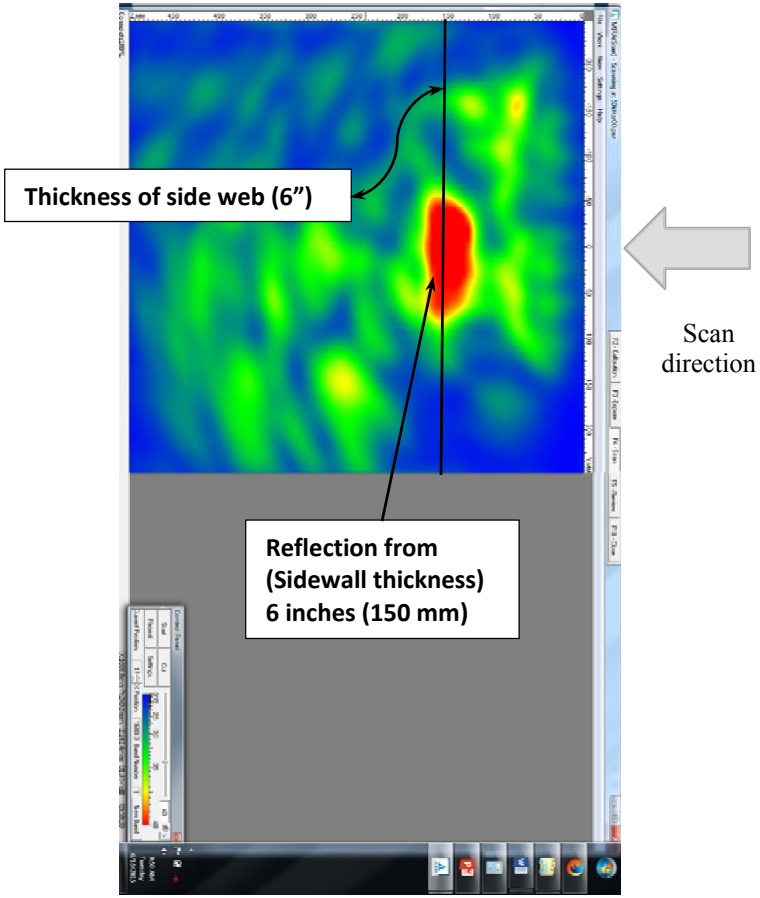

(a) Scan on web at 5’-8” (1700mm), 50 kHz, 40dB

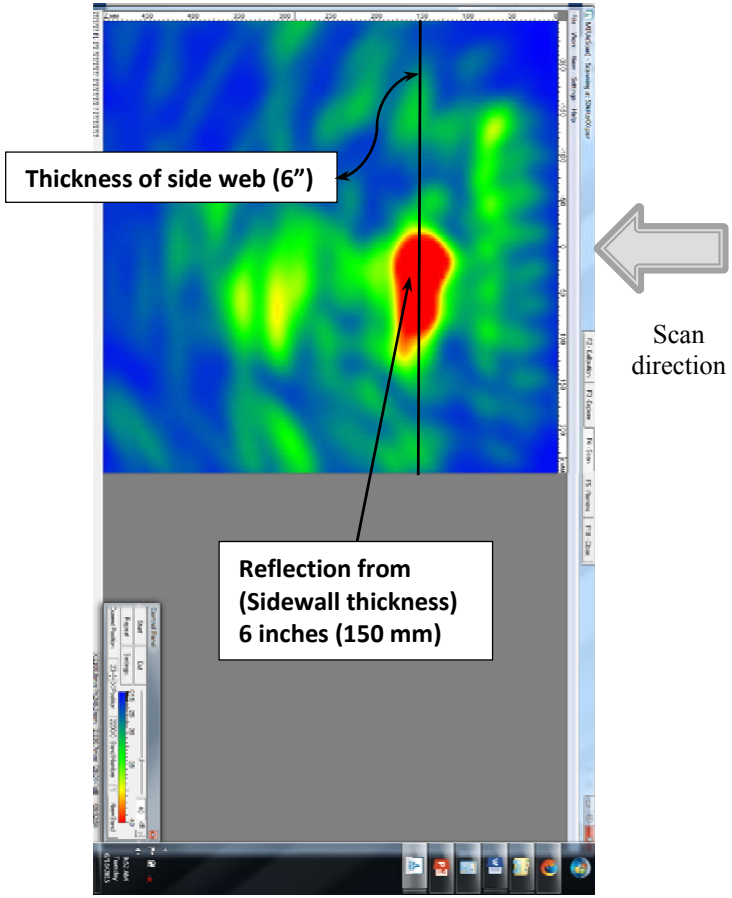

(b) Scan on web at 7’-8” (2300mm), 50 kHz, 40dB

Fig 5.7 Typical scans from the side of box beam with scanned location reference to end of beam

5.1.2 Electrochemical Measurements on Box Beams

The average half-cell potential differences (corrosion potential) of the bottom strands of the three salvaged box beams were measured using CANIN based on the methodology presented in Section 3.5.2 of Chapter 3. Readings were taken along the bottom of the box beams, results showing the different measured potential differences in millivolts as well as their respective relative and cumulative frequency graphs for the three salvaged box beams have been color coded and shown in Figures 5.9 through 5.21. Locations with excessive spallings which were not accessible for measurement have been color coded black on the superimposed results of the potential maps along the length of the beams.

The average results for salvaged box beam 1 (J11) varied from -130mV which according to ASTM 876 has 5% chance of corrosion to -530mV which has visible evidence of corrosion. The average results for salvaged box beam 2 (H6) varied from +12mV which according to ASTM 876 has 5% chance of corrosion to -583mV which has visible evidence of corrosion. The average results for salvaged box beam 3 (A1) varied from +10mV which according to ASTM 876 has 5% chance of corrosion to -393mV which has a chance of 95% chance of corrosion. Test results for salvaged box beams have been shown on the potential maps depicted in Figures 5.9 through 5.21. Values of half-cell potential were used to analyze the chance of corrosion along the bottom of the salvaged beams using the ASTM C876 guidelines, as it is shown in Table 5.1

A review of the corrosion potential maps of the three salvaged box beams as can be inferred from the color coded regions of the potential maps indicates that, box beam J11 had the largest corroded regions. This was very evident from visual inspections conducted on the box beams, as it was noted that box beam J11 exhibited a significant amount of delamination, spalling and cracking with visible signs of corrosion stains. It has been shown in subsequent section of this chapter, that comparing the residual flexural strengths of the three salvaged box beams, box beam J11 had the lowest residual flexural capacity. “It is often necessary to use other data such as chloride contents, depth of carbonation, delamination survey findings, rate of corrosion results, and environmental exposure conditions, in addition to corrosion potential measurements to formulate conclusions concerning corrosion activity of embedded steel and its probable effect on the service life of a

structure" (Reference: ASTM Designation C376-09). Cumulative frequency diagrams have been shown for beams H6 and A1 to provide an indication of the magnitude of affected area".

Table 5.1: Interpretation of half-cell potential values as per ASTM C876

Potential difference (mV)	Chance of rebar being corroded
< -500	Visible evidence of corrosion
-350 to -500	95%
-200 to -350	50%
> -200	5%

Figure 5.8: Electro-chemical Half-cell of salvaged beam

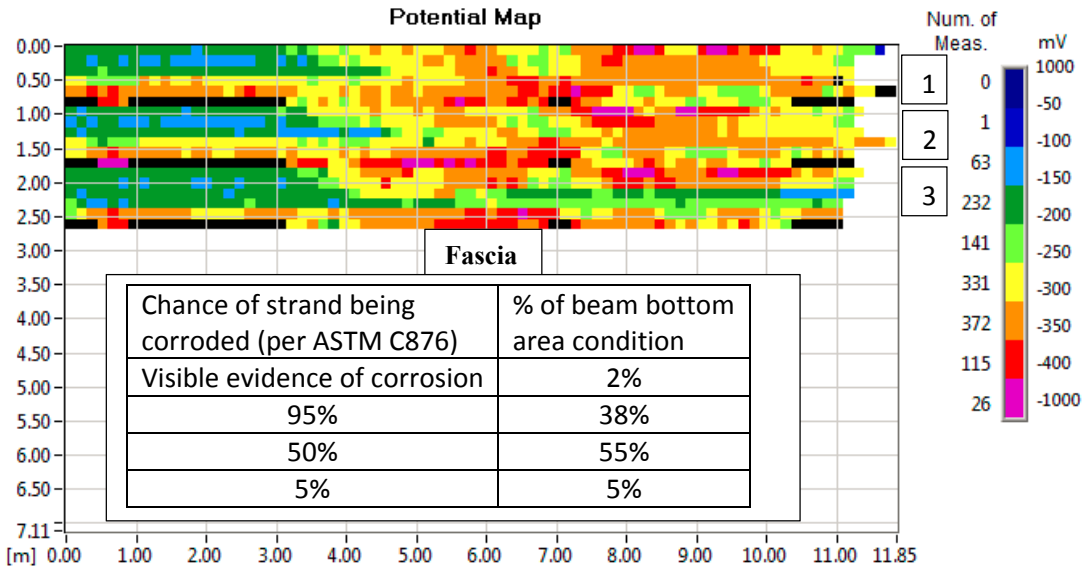

Chance of strand being corroded (per ASTM C876)	% of beam bottom area condition
Visible evidence of corrosion	2%
95%	38%
50%	55%
5%	5%

(1 meter = 3.28 feet)

Figure 5.9: Combined Electro-chemical Potential Map for Salvaged Beam 1 (J11), Test 1-3

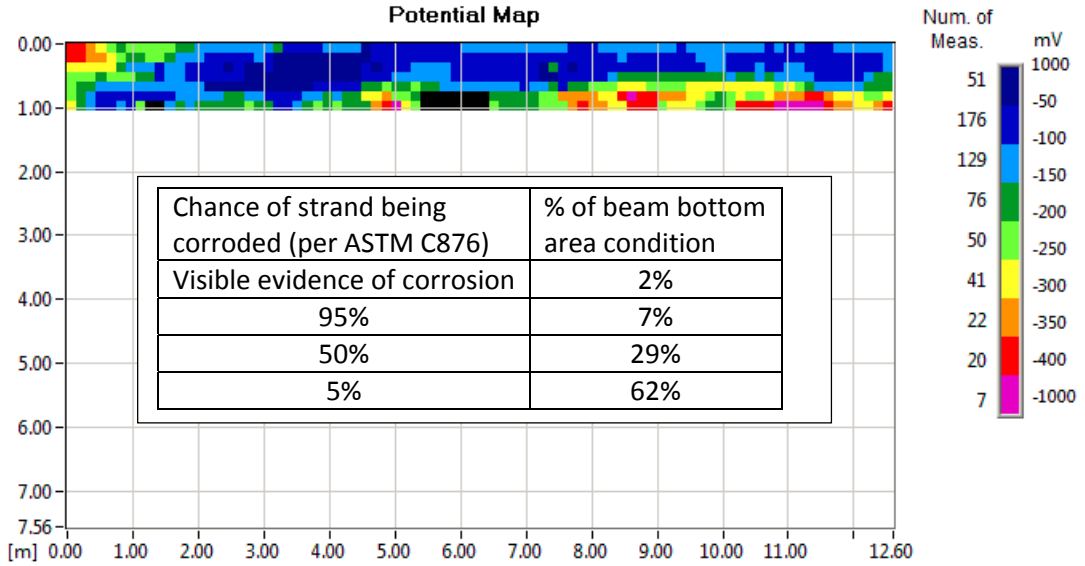

Chance of strand being corroded (per ASTM C876)	% of beam bottom area condition
Visible evidence of corrosion	2%
95%	7%
50%	29%
5%	62%

(1 meter = 3.28 feet)

Figure 5.10: Electro-chemical Potential Map for Salvaged Beam 2 (H6), Test 1

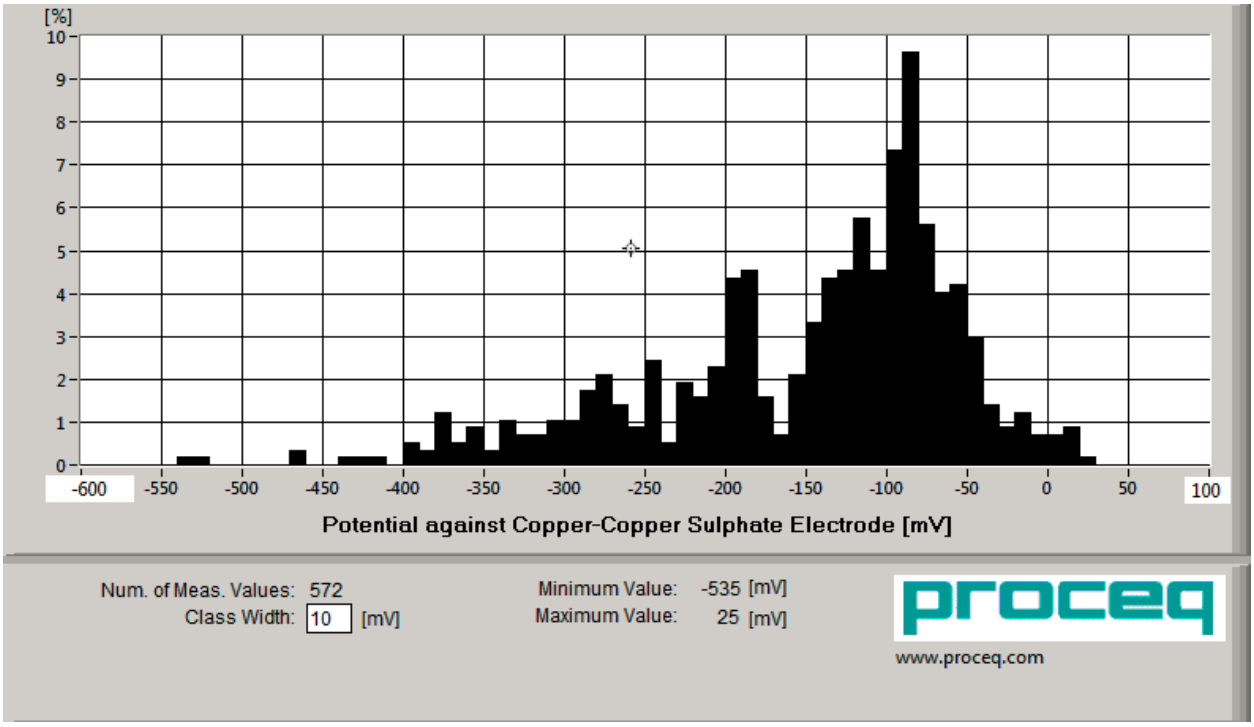

Figure 5.11: Relative Frequency for Salvaged Beam 2 (H6), Test 1

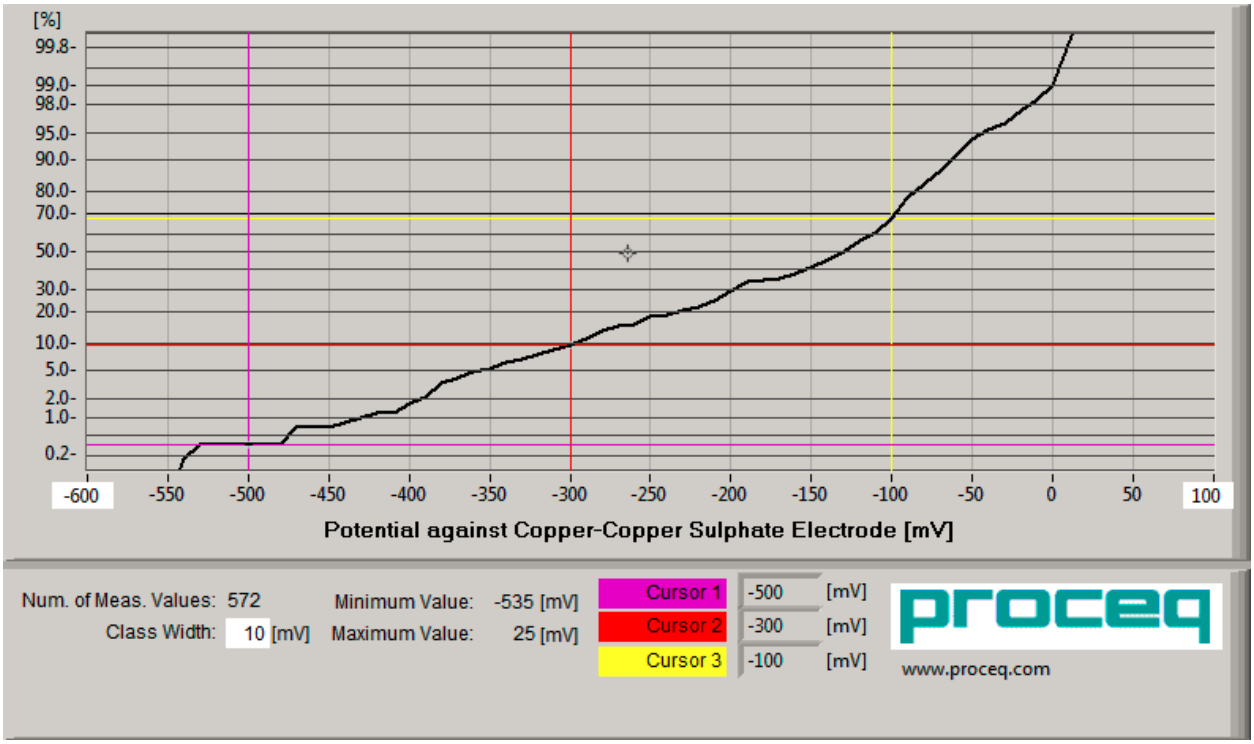

Figure 5.12: Cumulative Frequency for Salvaged Beam 2 (H6), Test 1

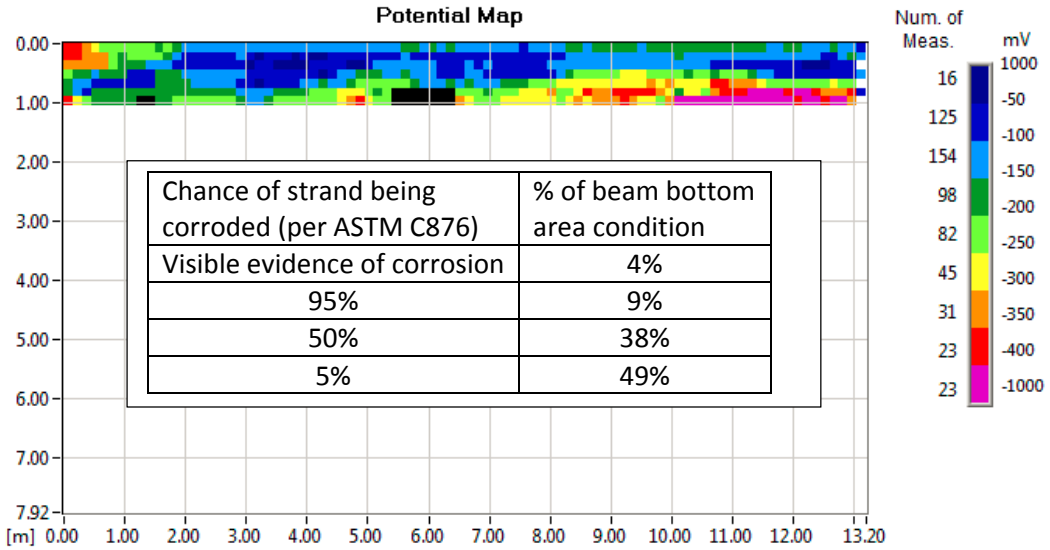

Chance of strand being corroded (per ASTM C876)	% of beam bottom area condition
Visible evidence of corrosion	4%
95%	9%
50%	38%
5%	49%

(1 meter = 3.28 feet)

Figure 5.13: Electro-chemical Potential Map for Salvaged Beam 2 (H6), Test 2

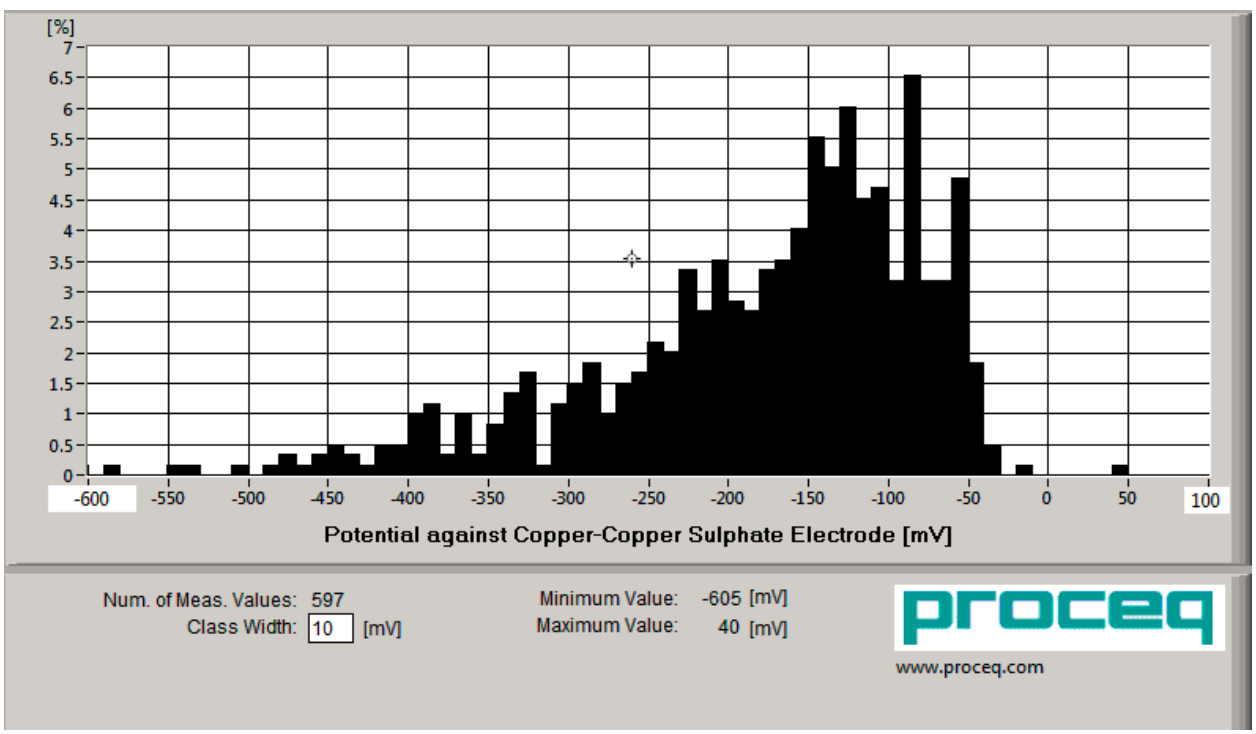

Figure 5.14: Relative Frequency for Salvaged Beam 2 (H6), Test 2

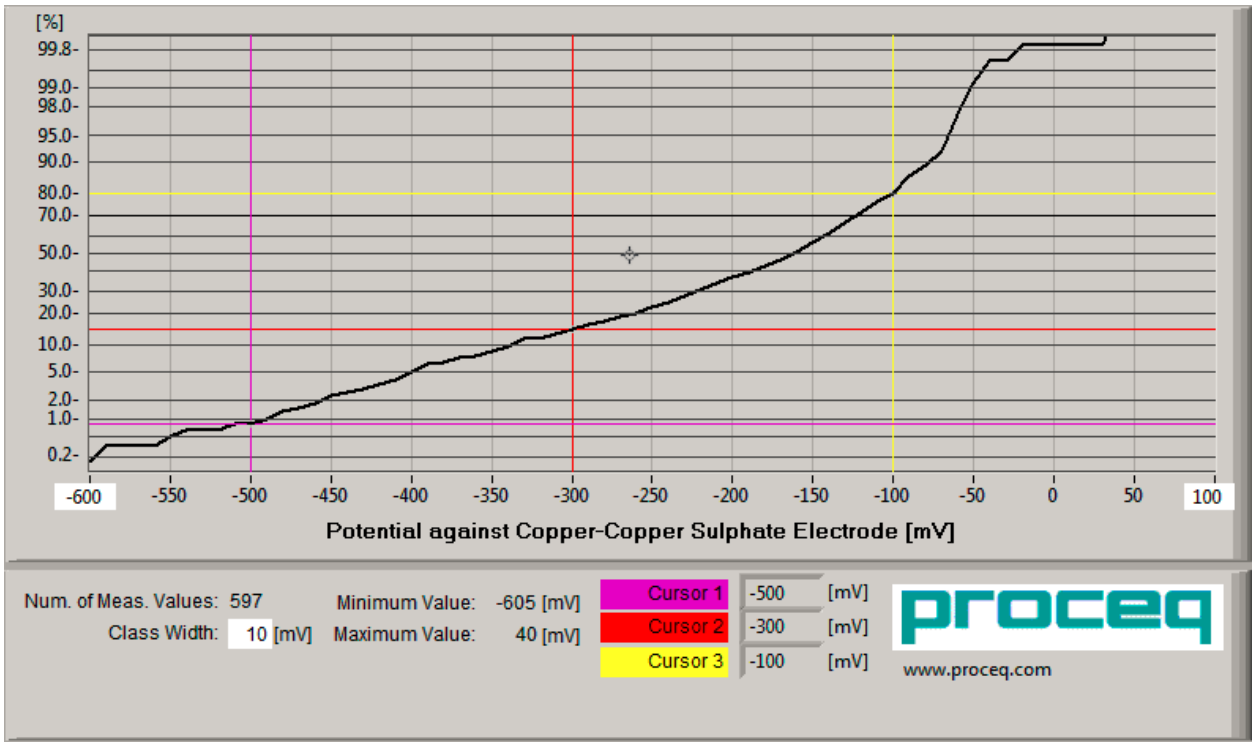

Figure 5.15: Cumulative Frequency for Salvaged Beam 2 (H6), Test 2

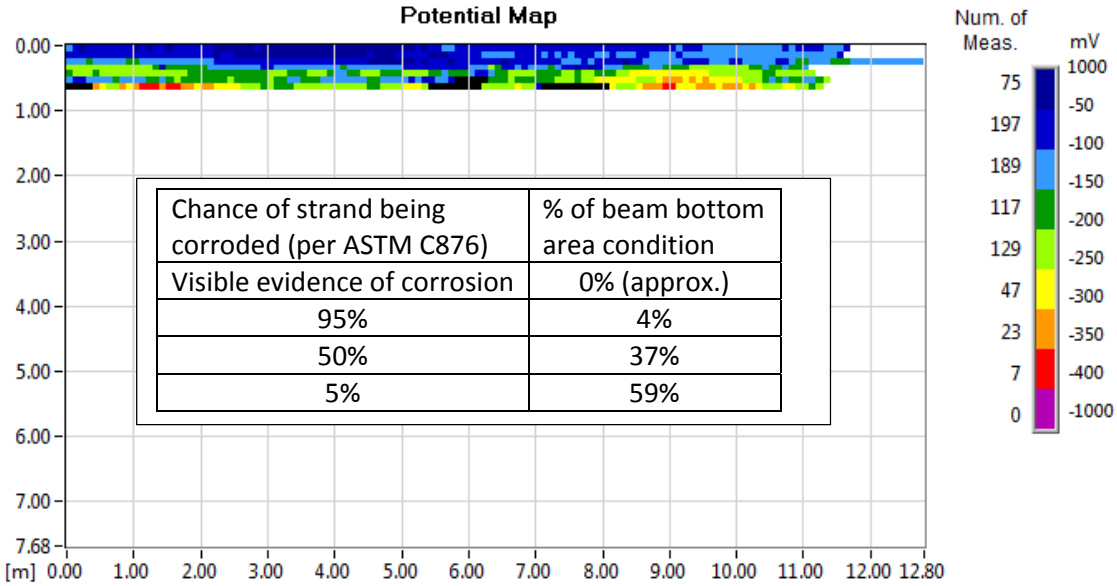

Chance of strand being corroded (per ASTM C876)	% of beam bottom area condition
Visible evidence of corrosion	0% (approx.)
95%	4%
50%	37%
5%	59%

(1 meter = 3.28 feet)

Figure 5.16: Electro-chemical Potential Map for Salvaged Beam 3 (A1), Test 1

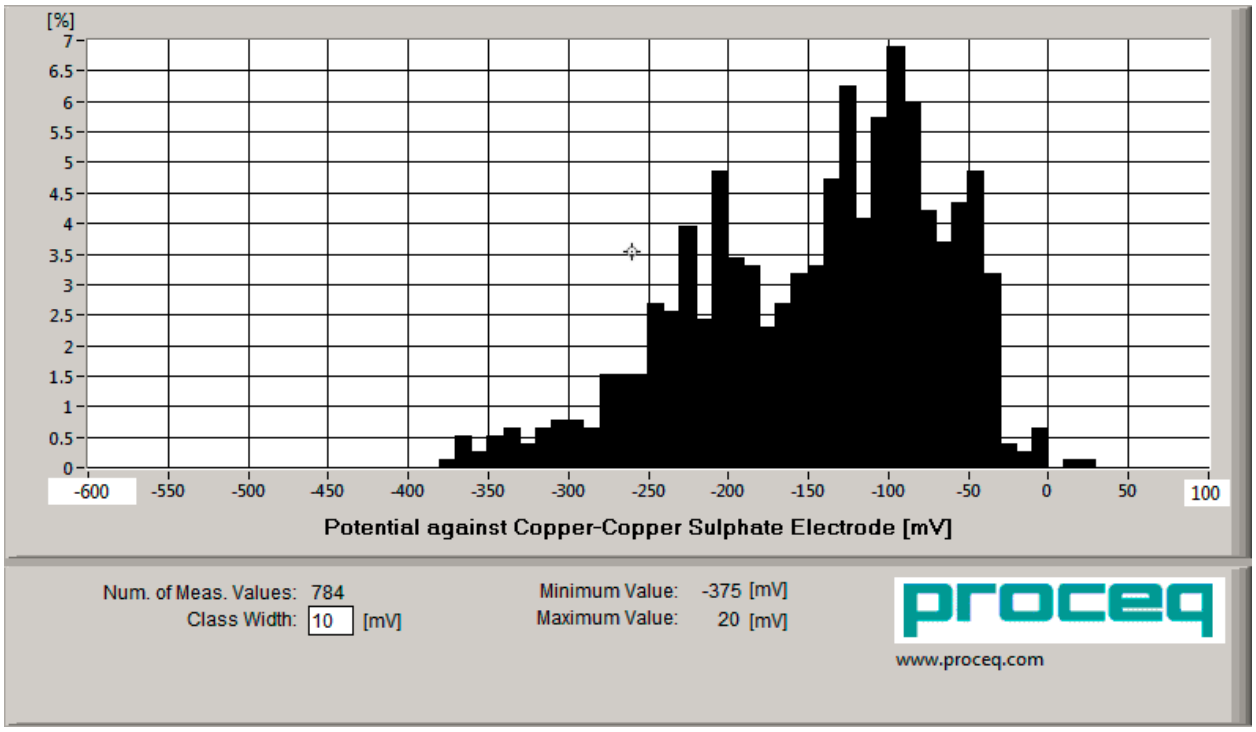

Figure 5.17: Relative Frequency for Salvaged Beam 3 (A1), Test 1

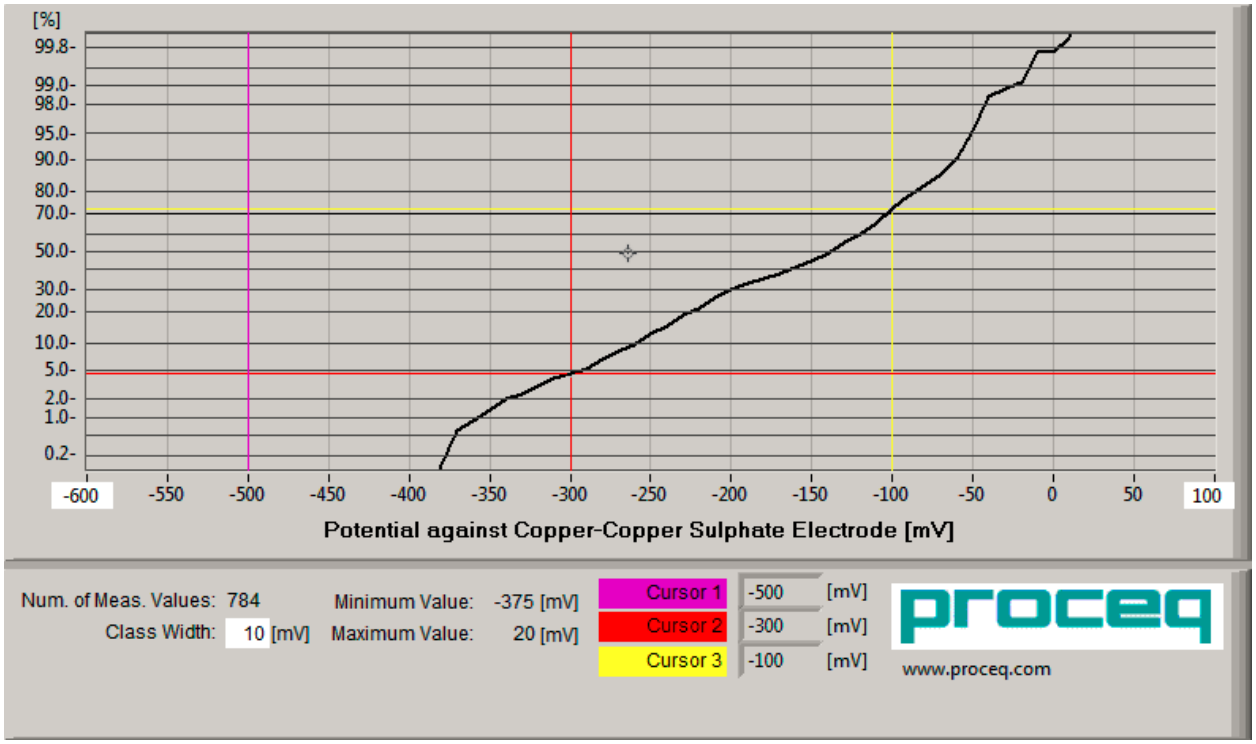

Figure 5.18: Cumulative Frequency for Salvaged Beam 3 (A1), Test 1

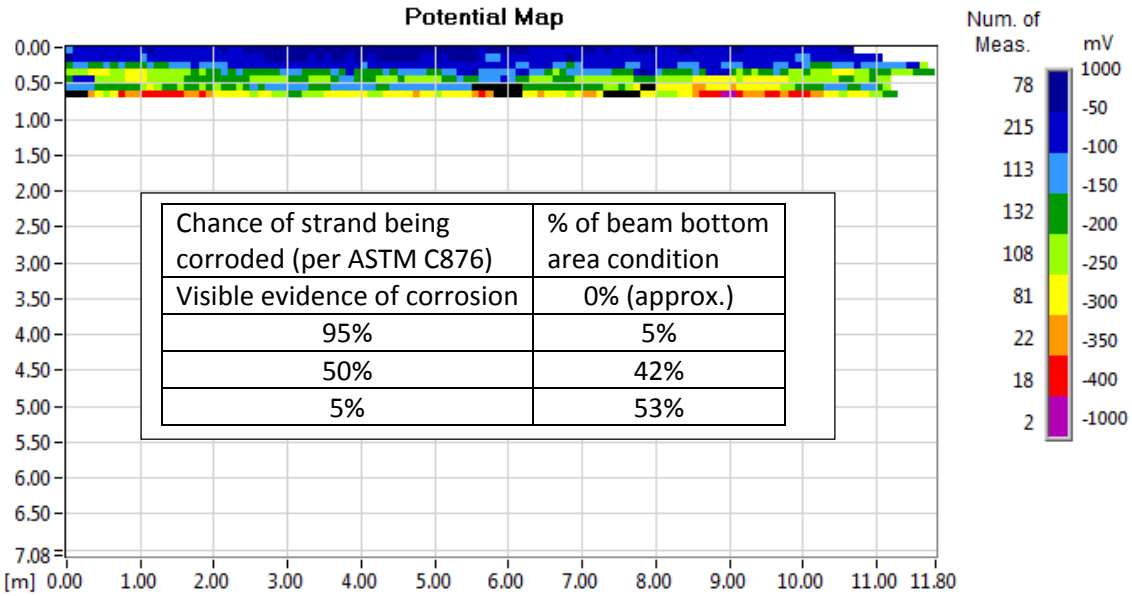

Chance of strand being corroded (per ASTM C876)	% of beam bottom area condition
Visible evidence of corrosion	0% (approx.)
95%	5%
50%	42%
5%	53%

(1 meter = 3.28 feet)

Figure 5.19: Electro-chemical Potential Map for Salvaged Beam 3, Test 2

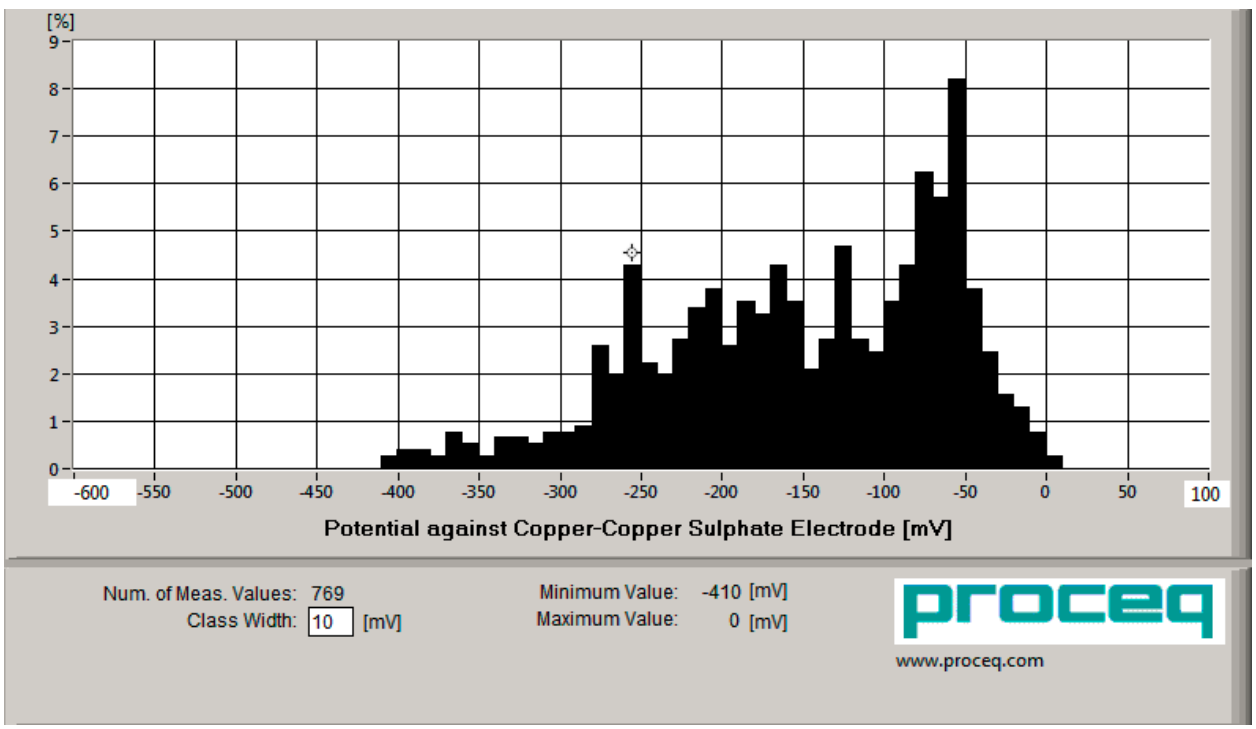

Figure 5.20: Relative Frequency for Salvaged Beam 3, Test 2

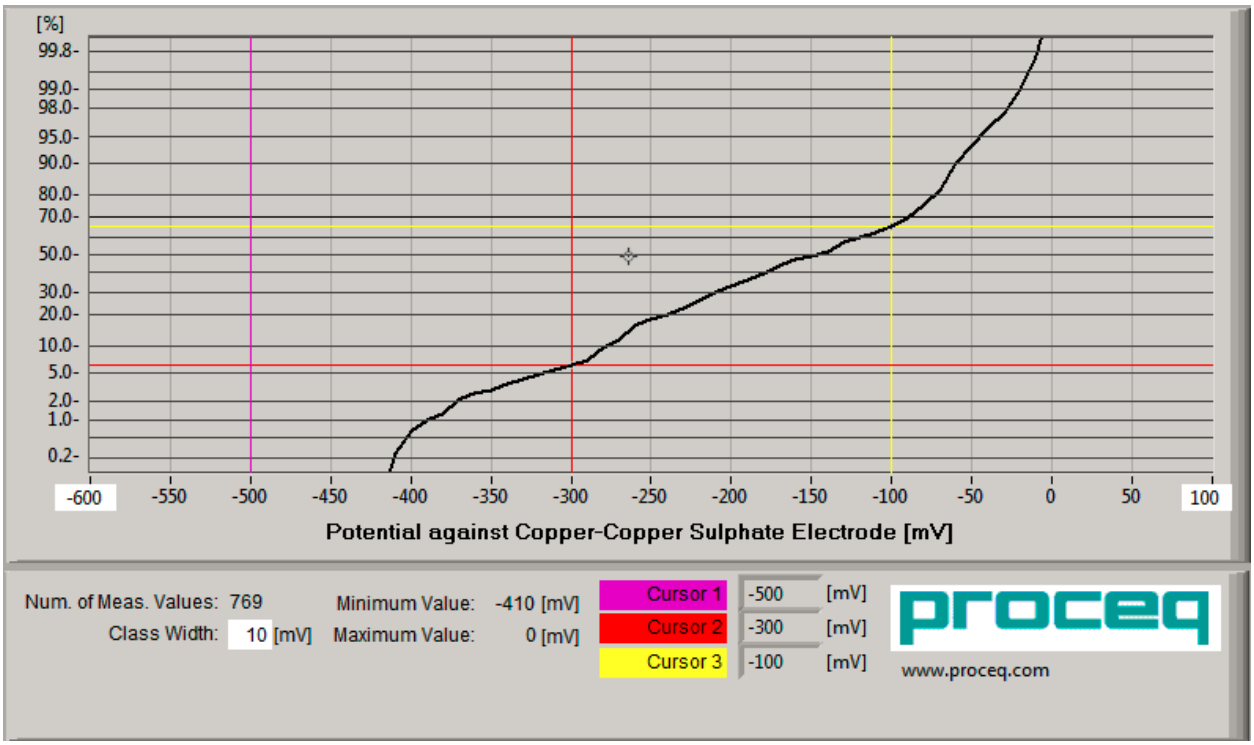

Figure 5.21: Cumulative Frequency for Salvaged Beam 3, Test 2

5.1.3 Impact Hammer Test on Box Beams

Grids of 6”x12” (150 mm-by-300 mm) were set-out along the bottom of the salvaged beams tested dividing the bottom surface into approximately 175 areas, and 10 measurements were taken within each grid. The method quantifies the rebound energy, Q value, of each area by taking the mean of 10 measurements per grid cell.

The hammer computer program “ProVista” relates the rebound coefficient/energy to the in-situ compressive strength. As the rebound value depends on the concrete in-situ hardness, the energy that the concrete absorbs can be correlated with its compressive strength. This relationship between energy absorbed and compressive strength is presented by a referencing curve, and in this project the curve used was the lower 10th percentile curve that comes with the instrument program. The following deductions were used: a low rebound number indicates that the concrete is weak, has low compressive strength. A high Q value indicates an intact surface and high compressive strength. An average in-situ compressive strength of 6,100 psi was estimated for the salvaged beams. This value represented the uncracked regions of the concrete. Figure 5.22 shows Schmidt hammer testing for salvaged box beam J11.

Figure 5.22: Schmidt Hammer Testing for Salvaged Beam 1.
Longitudinal cracking at both beam edges are visible on this photo.

5.1.4 Magnetic Flux Leakage Assessment of Salvaged Box Beams

Results and analysis of recorded signals for sensor M3 along selected strands of salvaged box beams J11, H6 and A1 have been summarized and presented below for a series of runs along each of the assessed strands. The selection of results to highlight was based on results from electro-chemical half-cell assessment shown above as well as observations made during visual inspection. Signals from sensor M3 along each of the evaluated strands were superimposed to obtain a combined effect of signal profile as shown on M3 Consolidated graphs for J11, H6 and A1 (Figures F-1 through F-20, Appendix F)

Moreover, an average signal amplitude between selected stirrups were superimposed on M3 Consolidated graphs data for each of the runs to normalize the effects of stirrups. The resulting graphs were M3 Adjusted graphs for J11, H6 and A1 (Figures F-2, F-4, F-6, F-8, F-10, F-12, F-14 and F-16). Sample calculations of estimated cross-sectional area losses along strand 4 of the north half of beam J11 have been presented below. Subsequent estimated cross-sectional area losses for the selected strands for the remaining halves of the box beams have been tabulated in Table 5.2. The estimated percentage cross-sectional area losses for beam J11 and H6 for the selected strands at designated locations have been tabulated in Table 5.2. Beam J11 had cross-sectional area losses ranging from 8% to 49% and H6 had losses ranging from 12% to 50%.

It should be emphasized that the MFL system was developed in parallel to the laboratory investigation of the salvaged box beams. The MFL was in the very early stages of development during testing of J11 (the first beam to be evaluated). The results of this entire assessment as well as the evaluation presented in Chapter 4 aided in the overall evaluation of the magnetic flux leakage system to estimate (quantify) cross section loss, and laid the foundation for future field pilot testing. Estimated cross-sectional area losses along the various selected strands for box beams J11 and H6 have been summarized in Table 5.2. MFL graphs of signal amplitude against distance for the selected strands used in the estimation of data shown in Table 5.2 have been shown in Figures F-1 through F-16. Figures F-17 through F-20 show MFL graphs of M3 consolidated graphs of strands 4 and 8. It should be noted that cross-sectional area losses estimation was not done for box beam A1. Box beam A1 was fairly in good condition from visual inspection, electro-chemical half-cell assessment as well as results obtained from flexural testing. The M3 consolidated graph

for selected strands of A1 was done to be compared with graphs of J11 and H6 to see if there were any hidden localized cross-sectional area losses along those strands. Some of the graphs show large fluctuations getting to the middle of the various assessed beams due to large cross-sectional area losses. Most graphs show very irregular signal amplitudes at the state of the assessments due to closely space stirrups. Typical cross-section of box beams J11, H6 and A1 have been shown in Figure 5.23, strand numbering were considered to start from the right bottom the box beam.

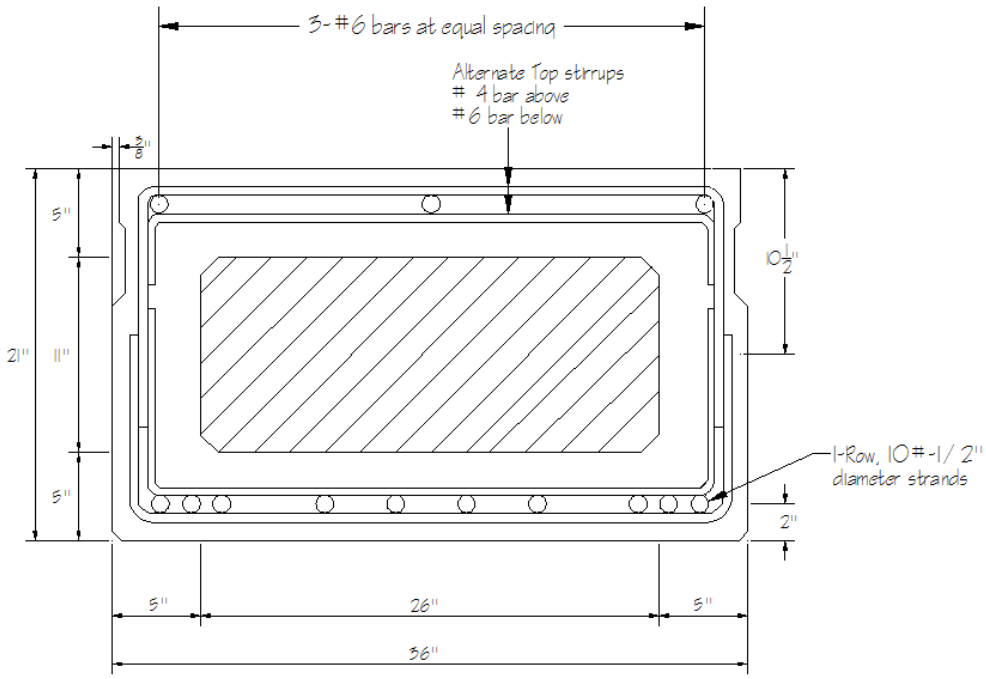

Figure 5.23: Typical Cross-section of Salvaged Beams

(Generated from construction drawings provided by Kent County Road Commission for Plainfield Bridge No. 6, Plan Sheet. 1074-3)

5.1.4.1 Estimation of Cross-sectional Area Loss

Considering strand 4 of North half of beam J11 (South to North direction), see Figure E-2

Average +ve signal amplitude between stirrups 3 and 4 = 4.9 mV

Location A (33.07 inches from 0)

Average +ve signal amplitude = 14.7 mV

Change in signal amplitude = 14.7 – 4.9 = 9.8 mV

Using the generated quadratic equation: $y = 0.0263x^2 - 0.1976x + 2.9222$

where:

x = cross-sectional area loss in sq. inch

y = change in signal amplitude in milli-volts (see Figures 4.17 and 4.18) due to cross-sectional area loss and stirrup effect, eliminating the constant, the quadratic equation becomes $y = 0.0263x^2 - 0.1976x$.

Substituting the value of y gives an approximate cross-sectional area loss of 0.0499 in^2 considering a cross-sectional area of 0.153 in^2 for 0.5 in diameter strand, the approximate percentage loss in cross section is 33%.

Location B (142.32 inches from 0)

Average +ve signal amplitude = 19.6 mV

Change in signal amplitude = 19.6 – 4.9 = 14.7 mV

Using the generated quadratic equation: $y = 0.0263x^2 - 0.1976x + 2.9222$

where:

x = cross-sectional area loss in sq. inch

y = change in signal amplitude in milli-volts due to cross-sectional area loss and stirrup effect, eliminating the constant, the quadratic equation becomes $y = 0.0263x^2 - 0.1976x$.

Substituting the value of y gives an approximate cross-sectional area loss of 0.075 in^2 considering a cross-sectional area of 0.153 in^2 for 0.5 in diameter strand, the approximate percentage loss in cross section is 49%.

Notation for Table 5

SHBB: scanned halves of box beams

ECLD: estimated cross-sectional area loss location indicating scanned distance from starting point with respect to north and south halves

ECL: estimated cross-sectional area loss in square inches

EPCL: estimated percentage cross-sectional area loss

Table 5.2: Predicted Cross-sectional Area Loss

Beam	Strand Number	SHBB	ECLD (inches)	ECL (sq. inches)	EPCL (%)
J11	4	North half	33.07 (A)	0.050	33
			142.32 (B)	0.075	49
		South half	51.96 (A)	0.012	8
			98.92 (B)	0.025	16
	6	North half	158.75 (A)	0.064	42
			126.48 (B)	0.041	27
		South half	86.12 (A)	0.035	23
			73.52 (B)	0.050	33
H6	1	North half	56.30 (A)	0.026	17
			117.22 (B)	0.019	12
		South half	92.52 (A)	0.050	33
			(B)	-	-
	8	North half	117.52 (A)	0.076	50
			42.22 (B)	0.027	18
		South half	91.44 (A)	0.075	49
			143.21 (B)	0.034	22

*Cross-sectional area of 0.5” diameter strand = 0.153 in^2

5.1.5 Analysis of Residual Flexural Testing of Salvaged Box Beams

Nondestructive evaluation was conducted on the salvaged box beams prior to flexural testing. The nondestructive methods deployed were: ultrasonic assessment for delamination and void detection; electro-chemical half-cell assessment for detecting corrosive environment; impact hammer assessment of surfaces to detect variations and potential delamination and magnetic flux leakage to determine loss of cross sectional area of rebar and strands. Concrete deterioration was assessed mainly by visual inspection and using the impact hammer to assess the average in-situ compressive strength and relative stiffness of the salvaged beam.

5.1.5.1 Salvaged Beam 1 (J11)

The beam behaved in an elastic manner until approximately an applied load of 20.9 kips, this was found to be in fair agreement with the calculated theoretical cracking load of 19.2 kips after assuming 20 percent loss of cross-sectional area per strand with only eight strands actively engaged. The estimated 20% cross-sectional area loss was determine after failure of the box beam by measuring the diameter of a series of exposed strands and statistically determining their mean diameter. The beam exhibited decreasing flexural stiffness as the load increased, failure of the beam occurred at 31.2 kips with mid-span deflection of 6 inches. The theoretical yield and ultimate failure loads calculated based on similar assumption of 20 percent loss of cross-sectional area of strands were 26.7 kips and 29.5 kips respectively. Comparing the estimated ultimate failure load of 50.5 kips as at the time the beam was built to the residual flexural failure load of 31.2 kips at failure, it can be inferred that box beam J11 lost 38% of designed flexural capacity.

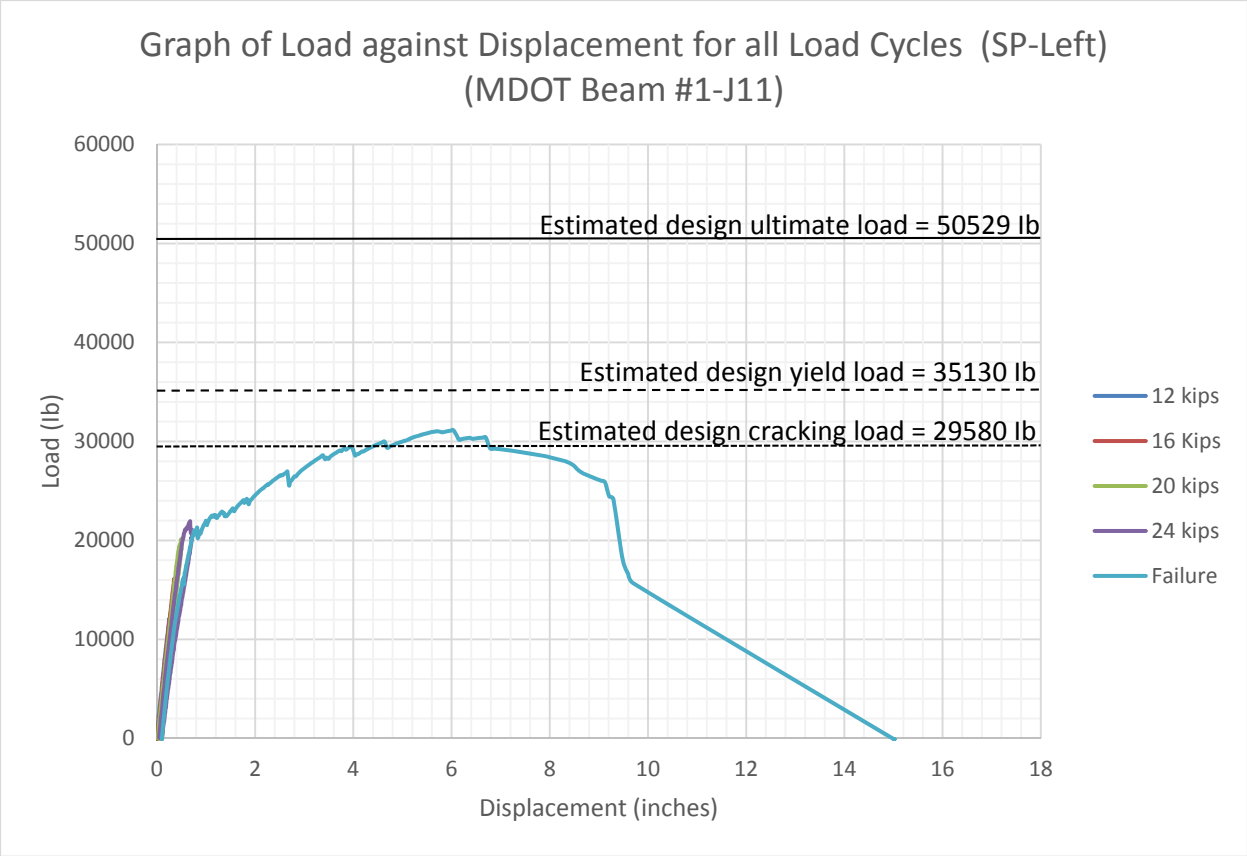

Figure 5.24: Graph of Load against Displacement for Salvaged Box Beam 1 (J11)

5.1.5.2 Salvaged Beam 2 (H6)

The beam behaved in an elastic manner until approximately 25.2 kips of load was applied, this was found to be in fair agreement with the calculated theoretical cracking load of 26.7 kips after assuming 10 percent loss of cross-sectional area per strand with all ten strands actively engaged. The beam exhibited decreasing flexural stiffness as the load increased, failure of the beam occurred at 37.0 kips with mid-span deflection of 9 inches. The theoretical yield and ultimate failure loads calculated based on similar assumption of 10 percent loss of cross-sectional area of strands were 35.1 kips and 44.9 kips respectively. Comparing the estimated ultimate failure load of 50.5 kips to the residual flexural failure load of 36.97 kips at failure, it can be inferred that box beam H6 lost 27% of designed flexural capacity.

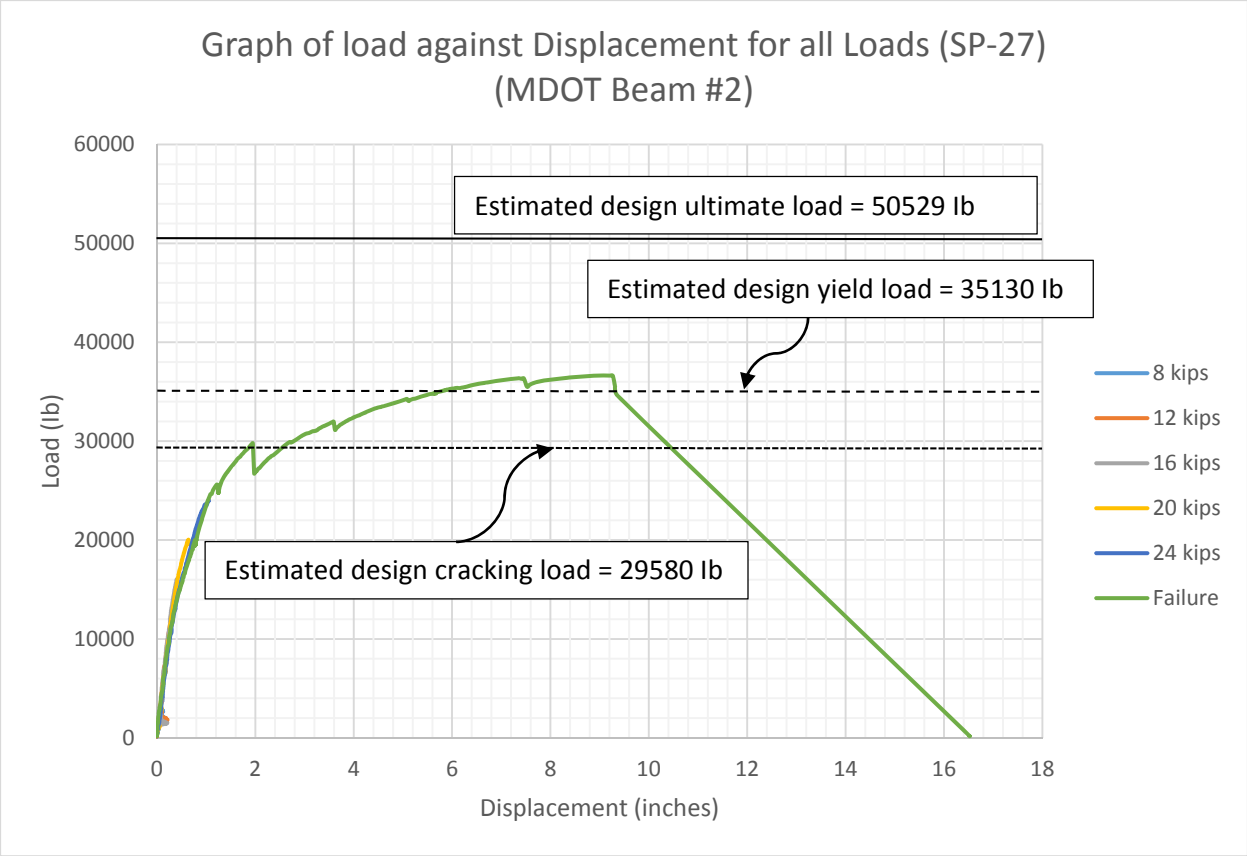

Figure 5.25: Graph of Load against Displacement for Salvaged Beam 2

5.1.5.3 Salvaged Beam 3 (A1)

The beam behaved in an elastic manner until approximately 30.2 kips of load was applied, this was found to be higher than the anticipated calculated theoretical cracking load of 26.7 kips after assuming 10 percent loss of cross-sectional area per strand with all ten strands actively engaged. The beam exhibited decreasing flexural stiffness as the load increased, failure of the beam occurred at 40.2 kips with mid-span deflection of 7.5 inches. The theoretical yield and ultimate failure loads calculated based on similar assumption of 10 percent loss of cross-sectional area of strands were 35.1 kips and 44.9 kips respectively. Comparing the estimated ultimate failure load of 50.5 kips to the residual flexural failure load of 40.16 kips at failure, it can be inferred that box beam H6 lost 21% of designed flexural capacity.

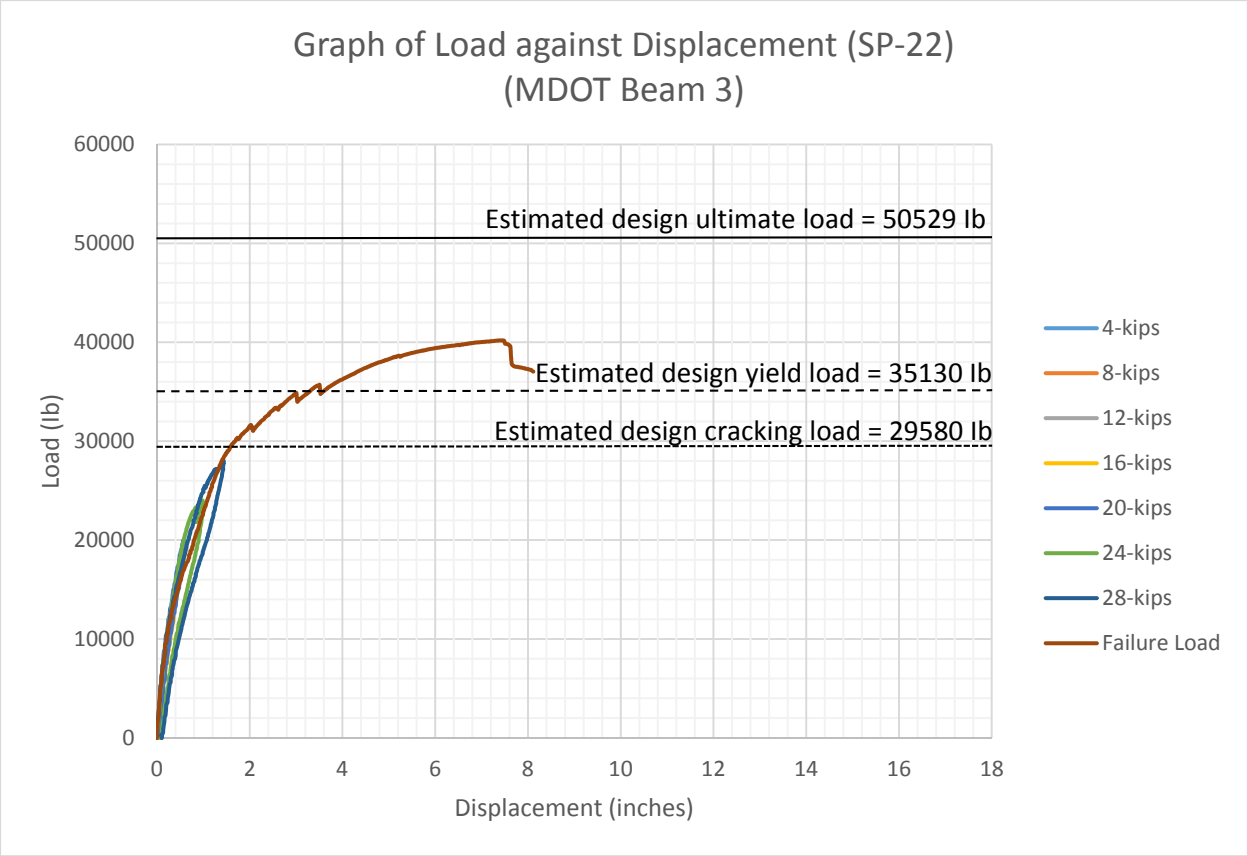

Figure 5.26: Graph of Load against Displacement for Salvaged Beam 3

5.2 I-96 Box Beams over Canal Road

Results of nondestructive testing conducted in the field on the two (2) fascia box beams along span 3 of bridge S08-55602 on beams with designations 3-A-8 and 3-M-11 have been presented below. The objective was to evaluate the chance of corrosion of the stirrups as well as to check the thickness of the web. This was necessitated as a result of excerpts from a consultant fabrication inspection report on bridge S08 that indicates that the internal box beam cell for some of the beams had shifted during casting, as detailed in Table 4 of Research Report TI-2027, by Structural Research Unit of MDOT reported in June, 2004. Furthermore, the exterior beams showed shear diagonal cracks near the supports.

At the time of this evaluation, August 2014, there were visible cracks along the exterior surface of 3-M-11. The crack widths, in the east tail span, measured in the range from 0.02 to 0.075 inches (0.5 to 1.9 mm) with additional hear line cracks. It could be inferred that the presence of these

cracks promoted corrosion of the stirrups as can been seen in Figure 5.29 with visible signs of corrosion stains. Crack mapping along the East tail span of the exterior section of 3-M-11 have been documented in Section 5.2.2..

5.2.1 Ultrasonic Assessment of I-96 Box Beams

Results of ultrasonic testing on the fascia webs of box beams 3-M-11 and 3-A-8 on the I-96 bridge conducted at a standard frequency of 50 kHz have been elaborated below. Scans were done along the length of the box beam as shown in Figure 5.27. The assessment of the side webs thicknesses were conducted to ascertain if the construction of these box beams were done in accordance with construction drawings. Reference plan sheets: Job No. 55602A, M-18 Eastbound over Canal Road, sheets (1 of 6) to (6 of 6). Reflection from side scans depicted that sections of 3-M-11 and 3-A-8 assessed conformed to construction drawings web thickness of 6" (150 mm). Reflections of scanned examples have been shown in Figures 5.28 (a) and (b).

Figure 5.27: Typical scan on the side of Box Beam 3-M-11

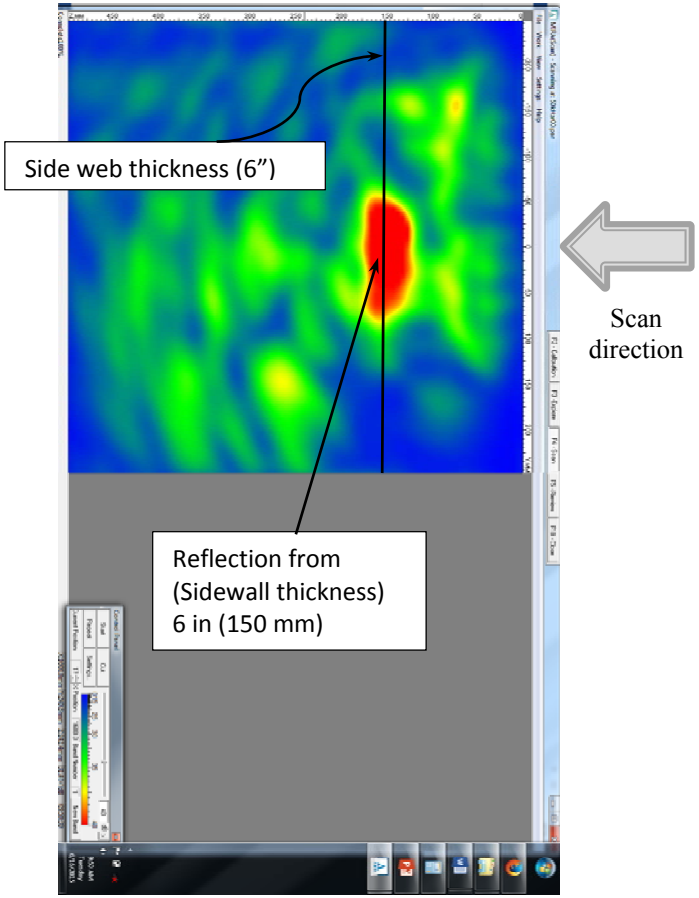

(a) Scan on web at (5’-8”) 1700mm.

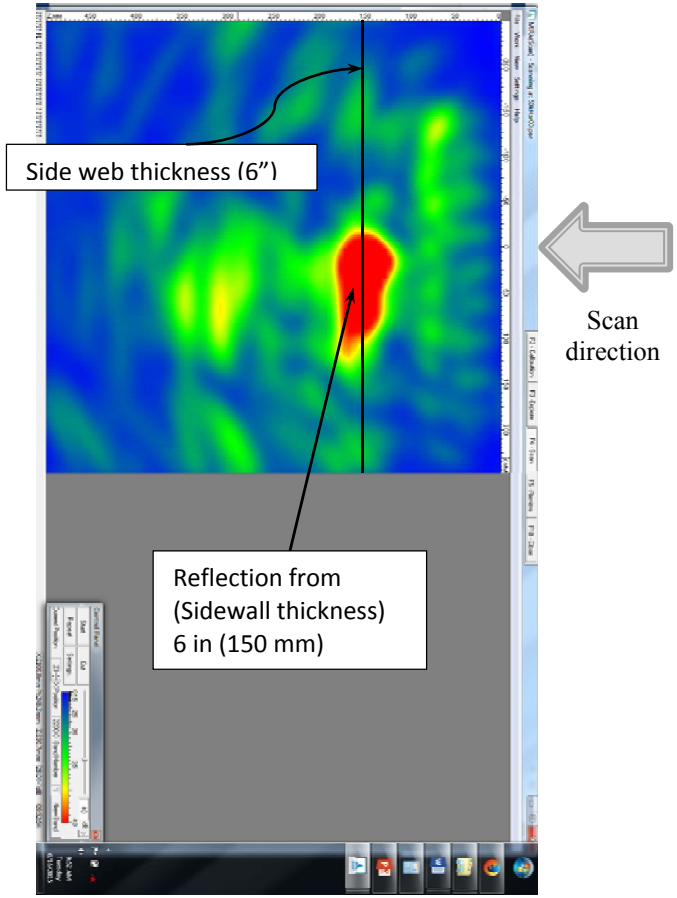

(b) Scan on web at (7’-8”) 2300mm

Fig 5.28 Typical scans from the side of box beam with scanned location reference to East end of beam

5.2.2 Electrochemical Half-cell Assessment of I-96 Box Beams

The average half-cell potential differences (corrosion potential) of the stirrups of the south fascia beam 3-M-11 is based on methodology presented in section 3.6.2.2. The test locations and recorded data have been shown in Figure 5.30. The average results have also been tabulated in Table 5.3. It can be deduced from Table 5.2 in comparison with Table 5.1 which has interpretation of half-cell potential values as per ASTM C876 that test location 4 with an average potential value of -349 mV has 50% chance of corrosion. Test locations 1, 3 and 5 through 9 had half-cell potential values ranging from -366 to -499, which according to ASTM C876 has 95% chance of corrosion. However, test location 2 had an average half-cell potential value of -556, per ASTM C876 had visible signs of corrosion. This was collaborated by visual inspection conducted along fascia beam 3-M-11 as can be seen from Figure 5.29 with evidence of corrosion stains along fascia beam during mapping out of stirrup locations using profometer.

It should be noted that a coating had been applied to the beams, and such coating can influence the results. However, considering the relative values of the half-cell potential differences and the corrosion stains it is very likely that active corrosion is occurring as a minimum at grid points 1, 2, 3, 5, and 6.

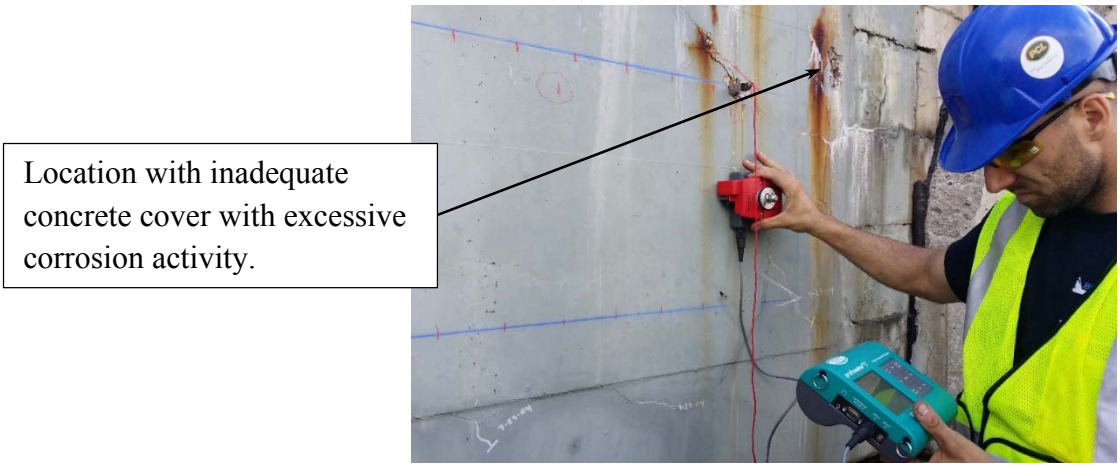

Figure 5.29: Mapping out of stirrup locations using profometer from abutment end towards the central pier locations, evidence of corrosion stains.

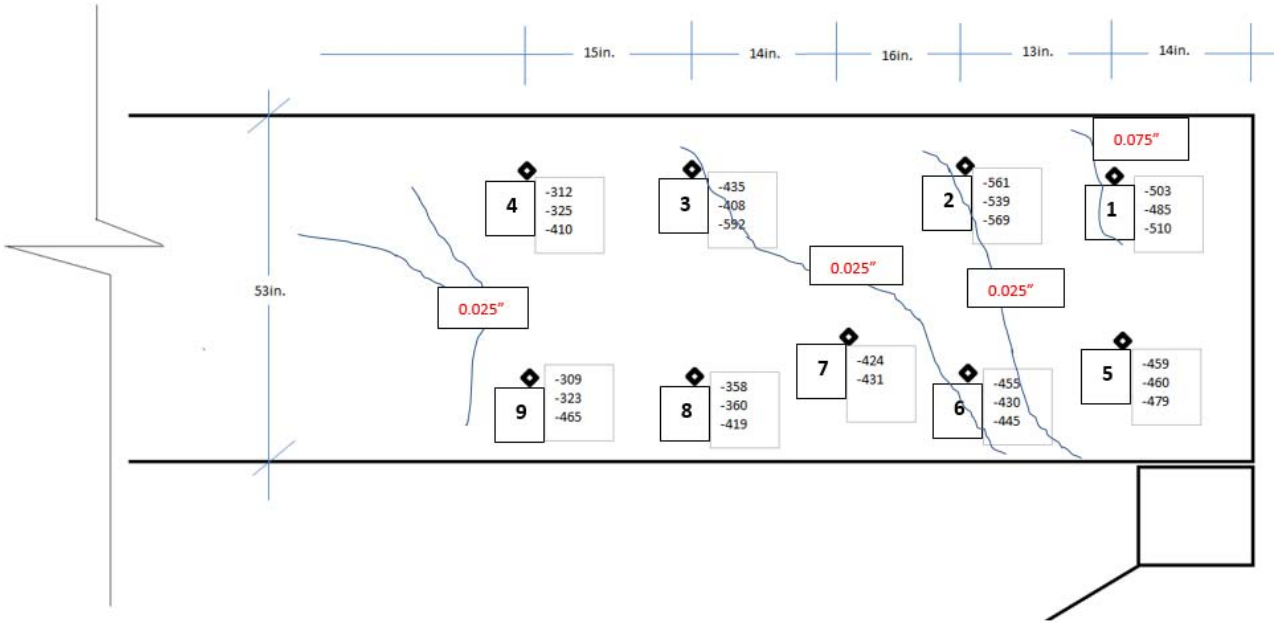

Figure 5.30: Test locations and recorded potential values along Fascia of 3-M-11. East tail support area is shown.

Table 5.3: Half-cell Potential difference along Fascia of 3-M-11

Points	1	2	3	4	5	6	7	8	9
Half-cell potential difference	-503 -485 -510	-561 -539 -569	-435 -408 -592	-312 -325 -410	-459 -460 -479	-455 -430 -445	-424 -431 -----	-358 -360 -419	-309 -323 -465
Average	-499	-556	-478	-349	-466	-443	-428	-379	-366

Interpretation of half-cell potential values as per ASTM C876

50% chance of corrosion	95% chance of corrosion	Visible evidence of corrosion

5.3 Segmental Box Beam Bridge carrying US-131 over Muskegon River.

Nondestructive assessment was conducted on sections of segmental box beam bridge carrying US-131 over Muskegon River, southbound lanes, 6 miles South of Big Rapids, MI. Ultrasonic assessment for delamination and void detection; electro-chemical half-cell assessment for detecting corrosive environment and magnetic flux leakage field pilot testing. The magnetic flux leakage deployment was conducted mainly to ascertain challenges of using the equipment in the field. The steel reinforcement mat in a floor segment was used for this purpose. Results and findings of assessment have been presented below. The field inspections were carried out from July 22-24, 2014. The following reference plan sheets were used: US-131 drawings from Job Number 16246A, Plan sheets: B01-1, B01-4, B01-5, B01-6 and B01-7.

Figure 5.31: US-131 over Muskegon River (SB)

Figure 5.32: US-131 over Muskegon River (SB) showing side elevation of segmental box beams

5.3.1 Ultrasonic Assessment

The following ultrasonic assessments were conducted along selected sections of the bridge carrying US-131 over Muskegon River.

- Ultrasonic assessments were conducted on transverse post-tensioned duct located in segments #2 and #4 from the north abutment.
- Ultrasonic assessment on longitudinal post-tensioned duct #24 between piers 1 and 2 and anchorage at ends of duct from north abutment.
- Ultrasonic assessment on selected bottom flange within segment #2 to support MFL field evaluation.
- Ultrasonic assessment on web within segment #2 along longitudinal and transverse rebar to check for pockets of void.

5.3.1.1 Ultrasonic Assessment on Transverse Post-tensioned Ducts in Segments 2 and 4

Results of ultrasonic assessment of ducts selected and located within segments 2 and 4 from north abutment have been presented below. Selected ducts were located using construction plan sheets referenced above and with the help of ground penetrating radar (MDOT operator). Ultrasonic assessment on transverse post-tensioning ducts were conducted at a standard frequency of 50 kHz. Scans were done perpendicular to the direction of the transverse post-tensioning ducts and were restricted to the interior portions of the segments. The length of scanning on each selected duct was approximately 21'-6" (6.55 m).

The scanned results from the transverse post-tensioned duct showed similar reflected scanned intensities with no significant differences. Examples of scanned results have been shown in Figure 5.35 (a) and (b). Therefore, it cannot be inferred that there is a change in grout condition or the presence of voids in the ducts. The scanned reflections at the location of the ducts shows there is change in density as the shear waves propagates through the top flange of the segment. It should be noted that the intensity of the reflection around the transverse duct is stronger than that observed in laboratory testing with both steel and plastic duct material (Chapter 4). The roadway surface did exhibit transverse cracks located over the transverse ducts as shown in Figure 5.34. However, it is unclear if these cracks are through thickness cracks.

Figure 5.33: Scanning on Transverse Post-tensioning duct within Segment #2

Figure 5.34: Transverse Road Surface Crack

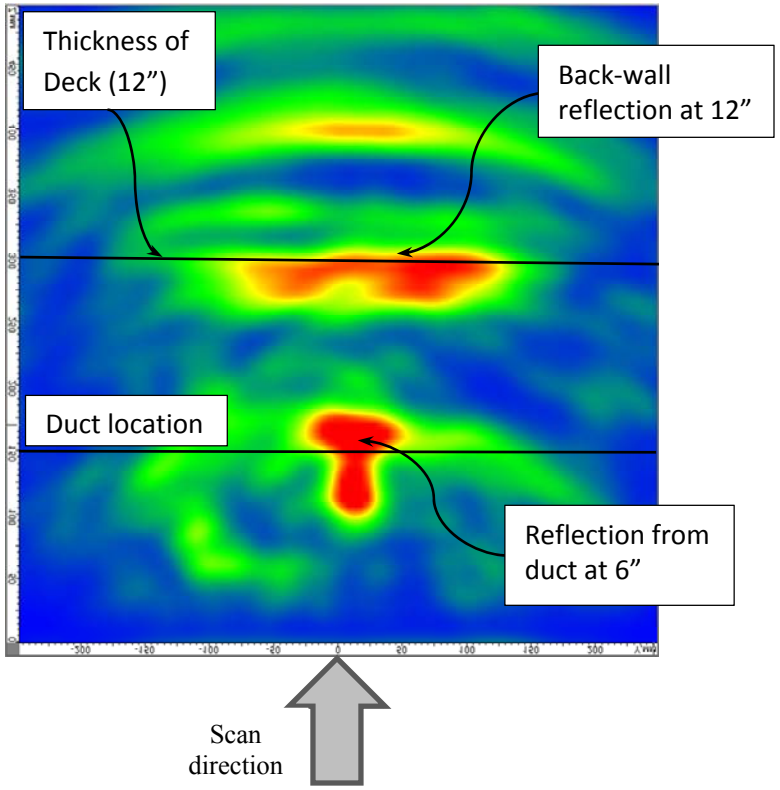

(a) Scan on transverse duct at (12’-8”) 3800mm

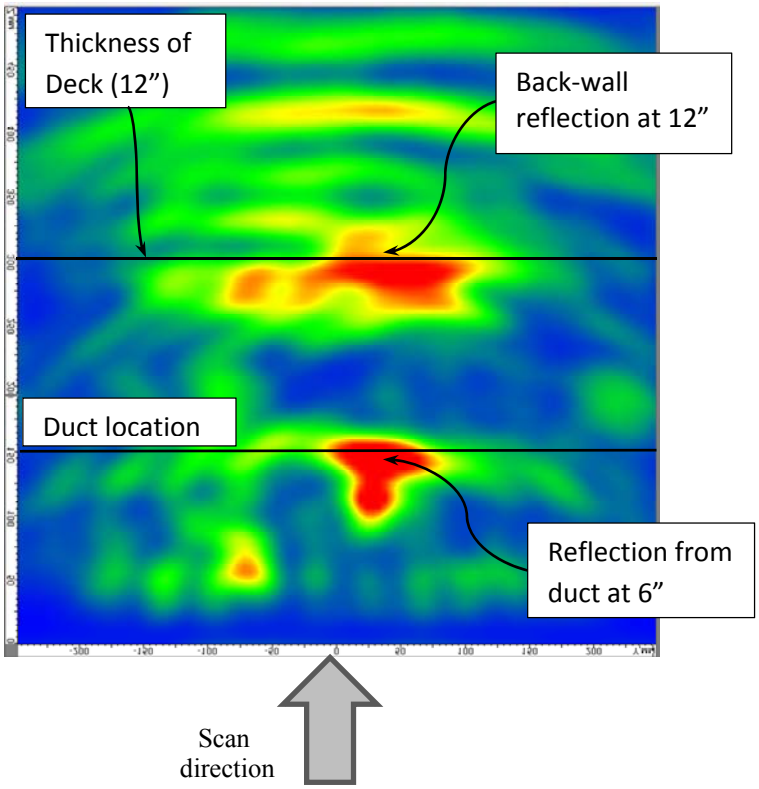

(b) Scan on transverse duct at (19’-8”) 5900mm

Fig 5.35: Typical scans from selected transverse post-tensioning duct within segment 2 from north abutment

5.3.1.2 Ultrasonic assessment on longitudinal post-tensioned duct #24 between pier 1 and 2 and anchorages at the ends of the duct.

Results of ultrasonic assessment along longitudinal post-tensioned duct #24 between pier 1 and pier 2 have been presented below. The selected duct was located using reference construction plan sheets and with the help of ground penetrating radar. All ultrasonic testing was conducted at a standard frequency of 50 kHz. Scans were done perpendicular to the direction of the duct.

Scan reflections along post-tensioned duct #24 show reflected intensities depicting the location of post-tensioned duct and the back-wall reflection indicating the thickness of the bottom flange at these scanned locations. The scan reflection intensities were very similar along the entire length of the duct. Therefore, a change in grouting/voids cannot be established. Recall from the analysis of the grouting defects simulated in the laboratory that reflected scanned intensities of scans taken before and after grouting had significant differences in scanned intensities conducted at the same locations with the same scanning frequencies and evaluated at the same decibels. However, reflected scanned intensities at the anchorage locations depicted multiple reflections apparently due to the congested reinforcement arrangement and potential honey-comb locations. Figure 5.39 (a) shows scan reflections from anchorage locations with multiple reflections around the post-tensioned duct compared to (b) depicting location of duct and back wall reflection without excessive multiple reflections.

Figure 5.36: Scanning on Longitudinal Post-tensioned Duct #24 and Anchorages at the ends.

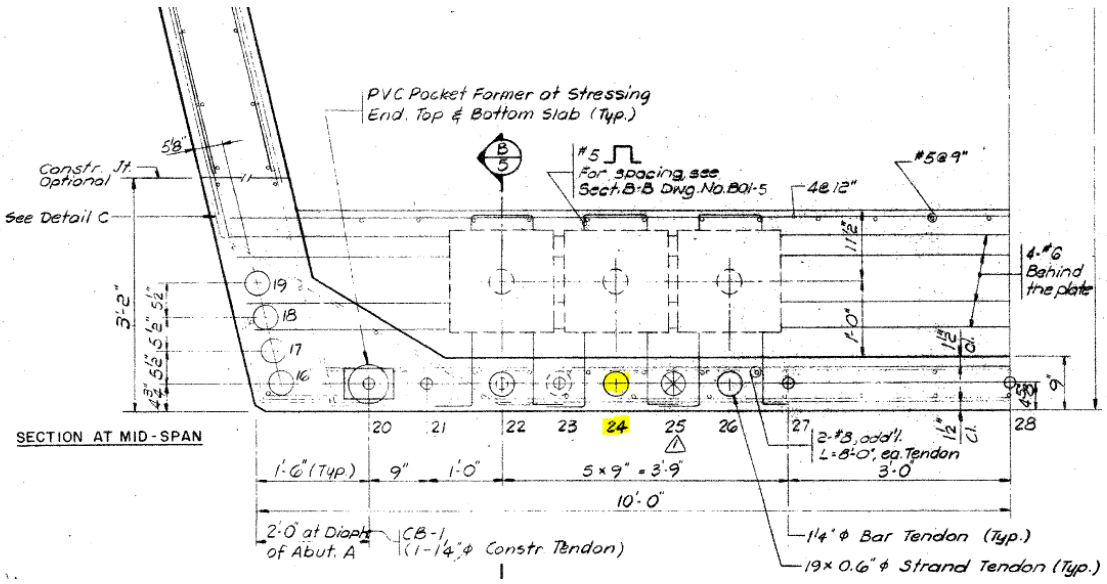

Figure 5.37: Cross-section of SB, showing Duct #24, Plan Sheet. BO1-4

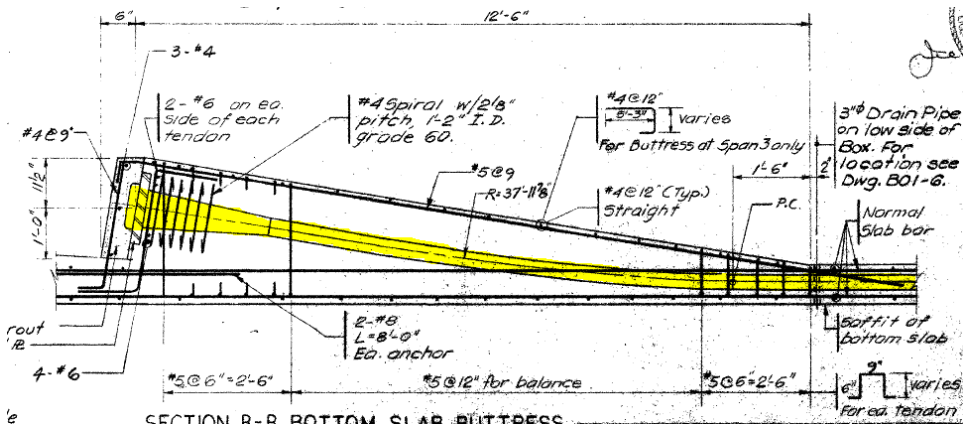

Figure 5.38: Tendon anchorage details for bottom slab, Plan Sheet. BO1-5

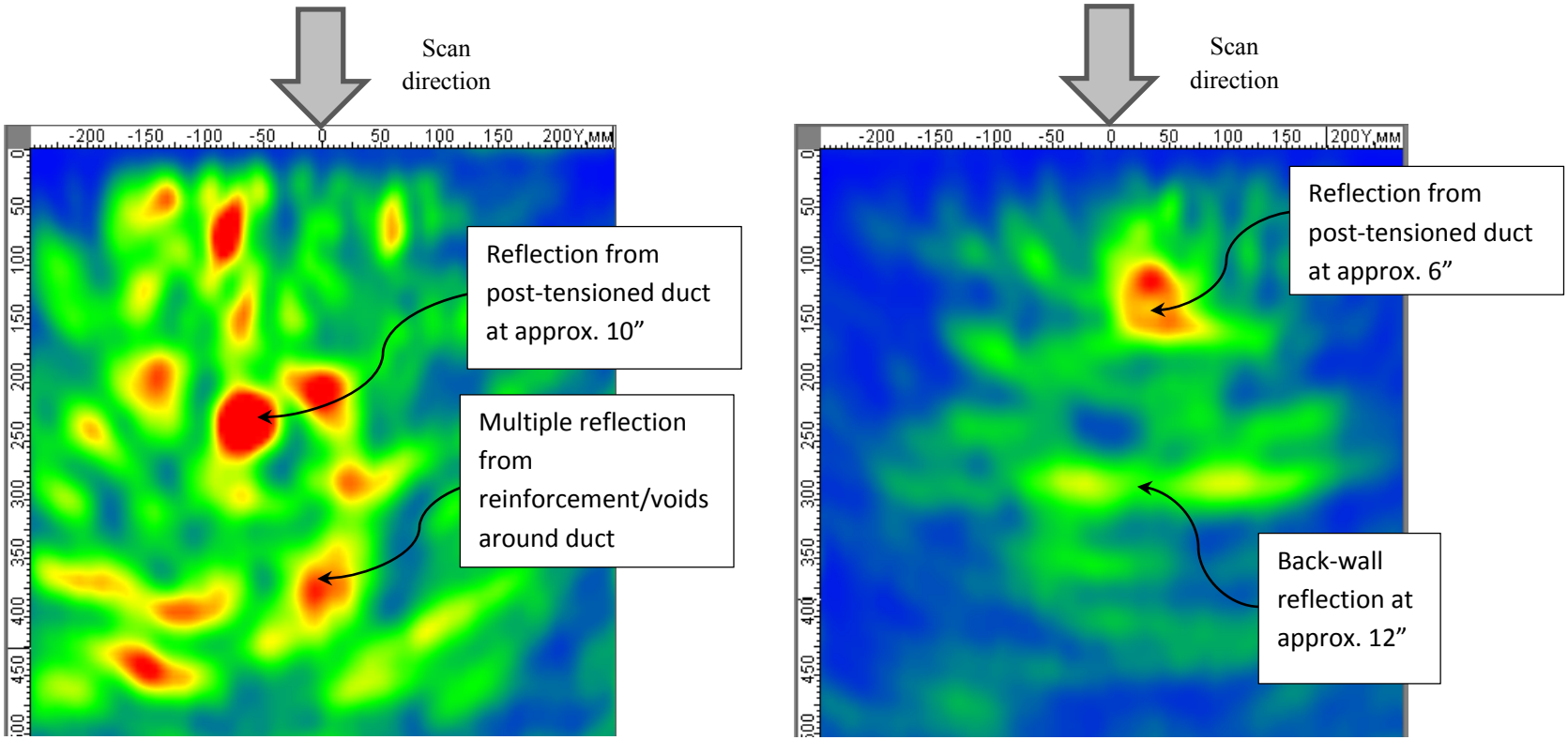

(a) Scan on anchorage duct with congested rebar *(b) Scan on longitudinal post-tensioned duct*

Figure 5.39: Typical scans along (a) anchorage location at (1’-4”) 400mm from anchorage end and (b) along longitudinal duct (22’-8”) 6800mm from anchorage end, assessment in north-bound direction.

5.3.1.3 Ultrasonic Assessment on Selected Bottom Floor within Segment #2

Results of ultrasonic assessment conducted on selected floor segment within segment #2 to support Magnetic Flux Leakage (MFL) pilot testing at the same location within segment #2 have been presented below. The test were conducted along grids mapped out along longitudinal and transverse top reinforcement of the bottom flange using US-131 Plan sheet from Job Number 16246A, plan sheet B01-7 and Ground Penetrating Radar. Scan results from the bottom floor conducted within segment #2 showed scanned reflections depicting reinforcement and back-wall reflections without multiple reflection around these reinforcement locations. Figure 5.42 show the results of one such scan. It can, therefore, be inferred that no voids could be detected in the bottom flange.

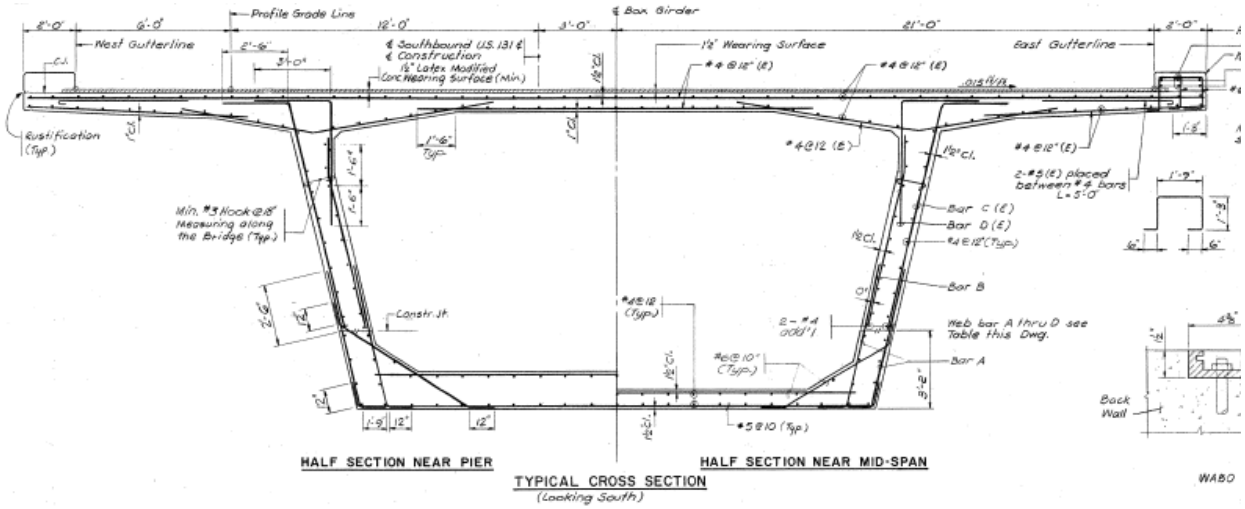

Figure 5.40: Typical Cross-section of Segment showing Bottom Flange and Web Reinforcement Details, Plan Sheet BO1-7

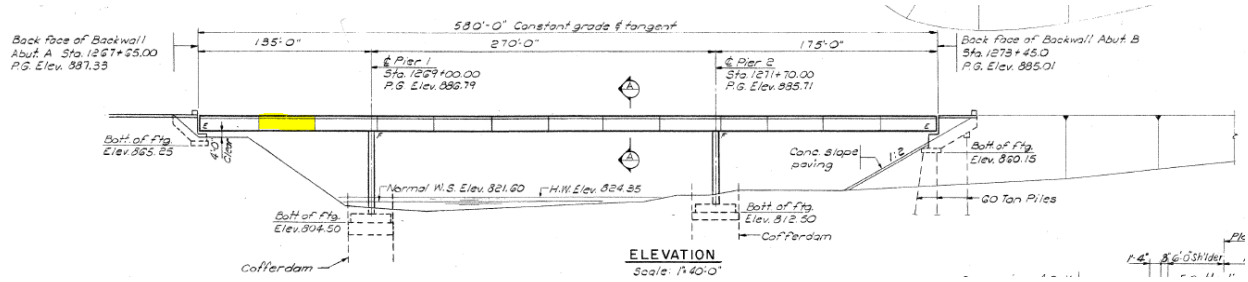

Figure 5.41: Segments arrangement showing location of segment #2 between abutment A and pier #1, Plan sheet. BO1-1

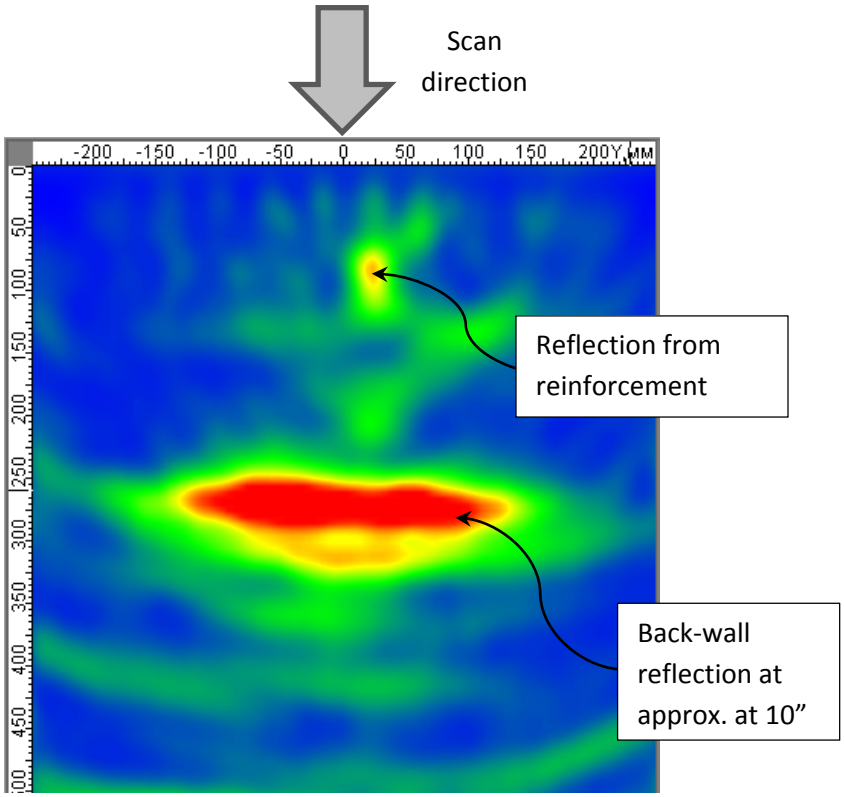

Fig 5.42 Typical scan along reinforcement, back wall reflection at 11 inches (275mm)

5.3.1.4 Ultrasonic Assessment on Web within Segment #2 along Longitudinal and Transverse Reinforcement to Check for Pockets of Voids

Ultrasonic assessment was conducted along selected section of the web, in segment 2, to evaluate if large pockets of voids and delamination around rebar could be detected, if present. The grids were mapped out using US-131 Plan sheet from Job Number 16246A, Plan sheet B01-7 and the ground penetrating radar. Scanning location was selected by visual inspection.

Scan reflections from the side web along reinforcement locations depicted pockets of voids around some of the scanned rebar. Typical examples of these scans have been shown in Figure 5.45 showing multiple reflections around the scanned rebar indicating voids. This was collaborated by visual inspection conducted before the ultrasonic assessment as has been shown in Figure 5.44. The figure shows the ultrasonic assessment location within segment 2 from the north abutment showing visible voids from the inner face of the web. The voids were caused by poor concrete consolidation. It is worth mentioning that the reflection intensity is significantly stronger around the reinforcement in the web than around the reinforcement in the well consolidated bottom flange (compare Figure 5.42 and Figure 5.45).

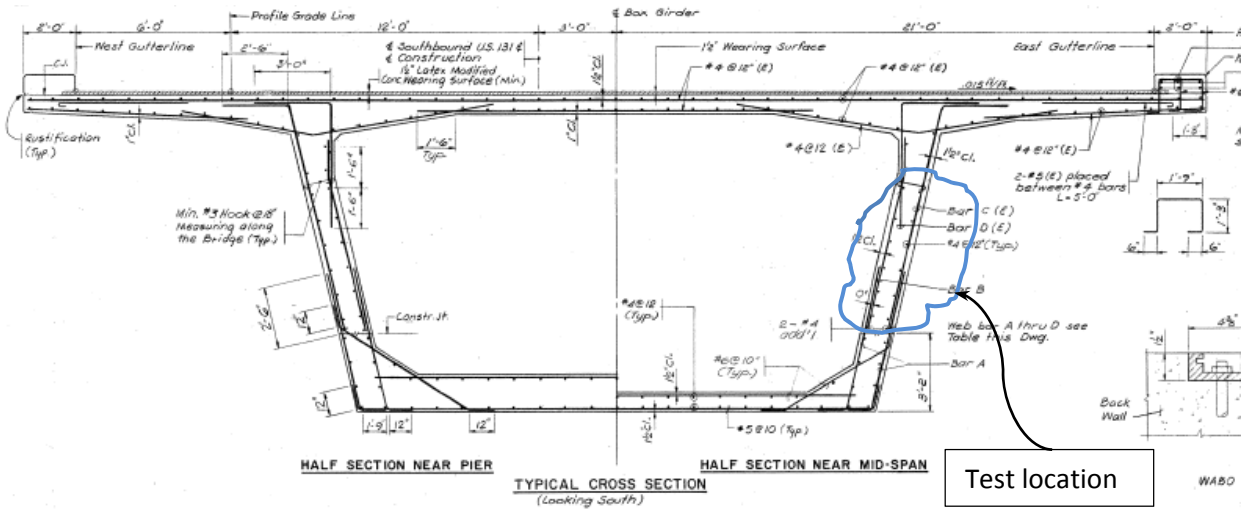

Figure 5.43: Typical Cross-section showing Test location along the Web of Segmental box beam, Plan Sheet BO1-7

Figure 5.44: Visible pockets of voids on inner surface of web.

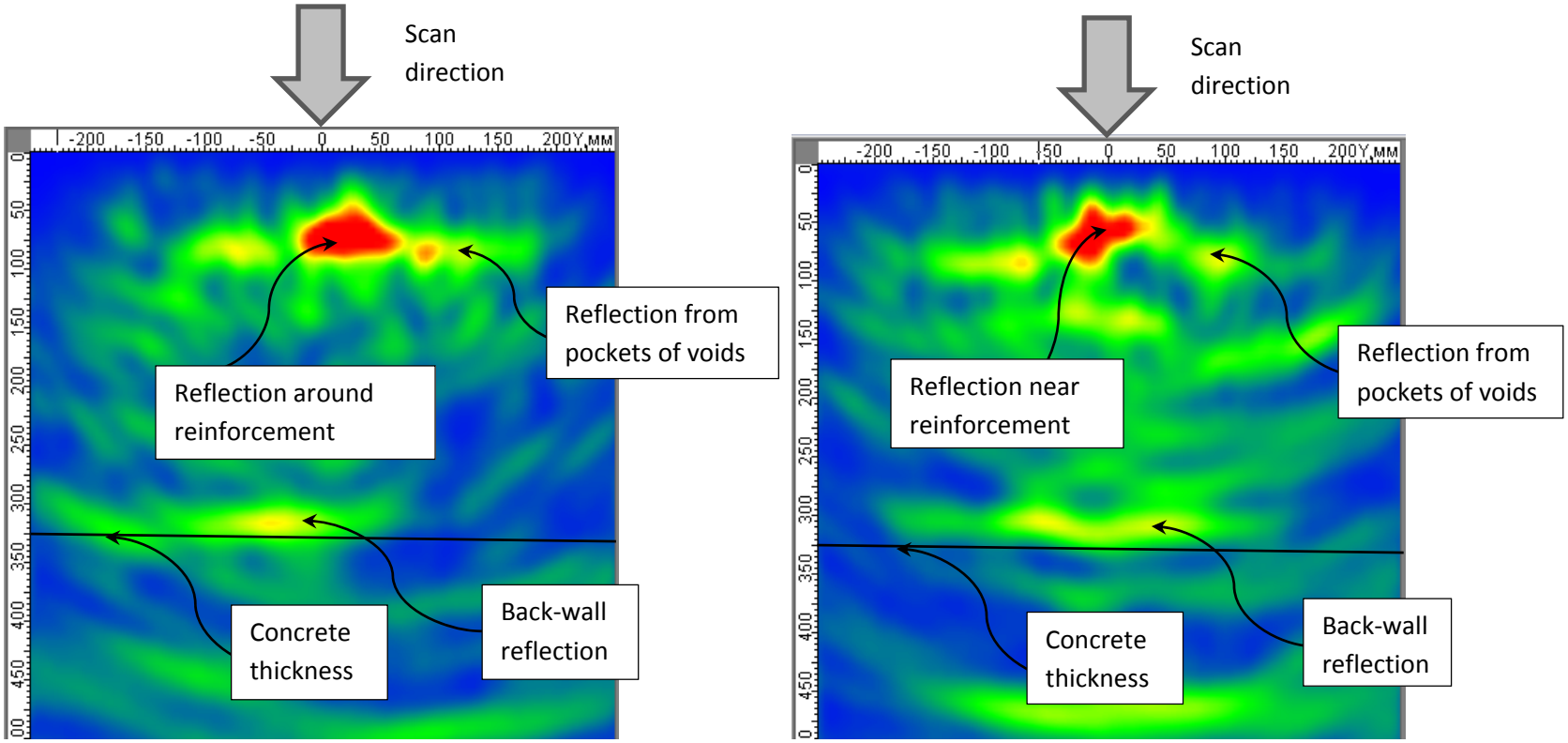

(a) Scan along reinforcement, showing pockets of voids. *(b) Scan along reinforcement, showing pockets of voids*

Fig 5.45: Typical scans along reinforcement showing pockets of voids around reinforcement from scans taken from side web within segment 2

5.3.2 Electrochemical Half-cell Assessment

Results of the average half-cell potential differences (corrosion potential) of the vertical and horizontal rebar of side web as shown on Figure 5.47 have been summarized below. There were two test areas (1 and 2) within segments 4 and 2, respectively. Figure 5.46 show half-cell potential testing within segment 2. The results of the half-cell potential measurements have been summarized in Tables 5.4 through 5.6 for test area 1 within segment 4 and Tables 5.7 through 5.9 for test area 2 within segment 2.

Test area 1, located in segment 4, was immediately adjacent to the pier support. The web in this area did exhibit diagonal cracking. Several of these cracks had been sealed earlier by MDOT. These seals were avoided during testing so that all measurements were taken on concrete surface. Test area 2 located further away from any support did not exhibit any significant cracking. Surface rust stains were not observed on the web in either test area.

It is worth mentioning that the absolute values of the half-cell potentials are higher than expected. However, due to the moist environment, being located over a river, could cause this offset. Yet, it is concerning that these large gradients are measured indicating that there are localized risks of corrosion near the pier support in particular.

Figure 5.46: Electro-chemical half-cell Assessment of selected Section of Web along Segment #2

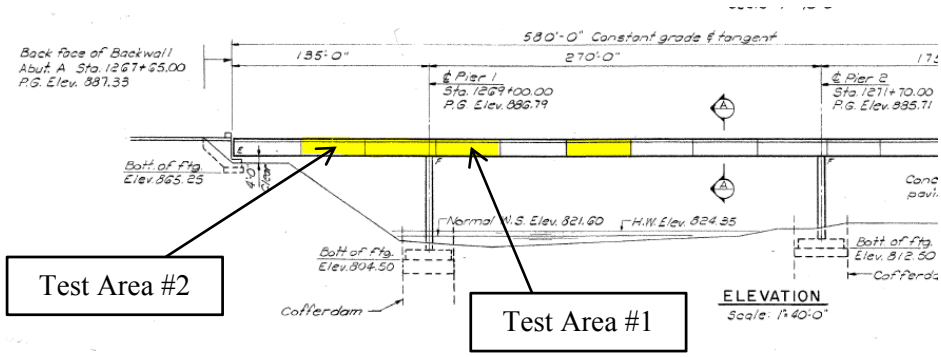

Figure 5.47: Layout of Southbound Bridge indicating Test Areas #1 and #2

Table 5.4: Half-cell potential difference data of Test Area #1

Axis	1	2	3	4	5	6	7	8	9	10
1	-241	-261	-248	-270	-342	-286	-315	-516	-240	-166
	-218	-208	-211	-260	-286	-721	-293	-530	-267	-200
	-285	-298	-258	-336	-412	-761	-373	-609	-328	-211
Average	-248	-256	-239	-289	-347	-589	-327	-552	-278	-192
2	-272	-388	-303	-313	-310	-271	-405	-335	-325	-211
	-295	-439	-280	-422	-278	-601	-499	-339	-339	-241
	-398	-304	-374	-530	-384	-755	-568	-457	-413	-323
	-322	-377	-319	-422	-324	-542	-491	-377	-359	-258
3	-261	-337	-504	-407	-628	-325	-381	-328	-232	-204
	-505	-314	-530	-385	-491	-311	-433	-314	-276	-246
	-379	-441	-620	-435	-593	-612	-504	-432	-289	-243
Average	-382	-364	-551	-409	-571	-416	-439	-358	-266	-231
4	-307	-673	-321	-719	-273	-425	-416	-615	-389	-492
	-294	-555	-321	-677	-242	-475	-433	-630	-404	-419
	-260	-607	-391	-688	-320	-335	-560	-641	-482	-574
	-287	-612	-344	-695	-278	-412	-470	-629	-425	-495
5	-258	-250	-240	-278	-233	-302	-294	-280	-223	-324
	-219	-188	-205	-225	-209	-312	-323	-337	-243	-288
	-275	-257	-276	-273	-254	-401	-390	-463	-289	-292
Average	-251	-232	-240	-259	-232	-338	-336	-360	-252	-301

Table 5.5: Average Half-cell potential difference data of Test Area #1

Axis	1	2	3	4	5	6	7	8	9	10
1	-248	-256	-239	-289	-347	-589	-327	-552	-278	-192
2	-322	-377	-319	-422	-324	-542	-491	-377	-359	-258
3	-382	-364	-551	-409	-571	-416	-439	-358	-266	-231
4	-287	-612	-344	-695	-278	-412	-470	-629	-425	-495
5	-251	-232	-240	-259	-232	-338	-336	-360	-252	-301

Table 5.6: Chance of rebar corrosion in Test Area 1

(Interpretation of results per ASTM C876)

Axis	1	2	3	4	5	6	7	8	9	10
1	50%	50%	50%	50%	50%	VEC	50%	VEC	50%	5%
2	50%	95%	50%	95%	50%	VEC	95%	95%	95%	50%
3	95%	95%	VEC	95%	VEC	95%	95%	95%	50%	50%
4	50%	VEC	50%	VEC	50%	95%	95%	VEC	95%	95%
5	50%	50%	50%	50%	50%	50%	50%	95%	50%	50%

VEC= Visible evidence of corrosion

Table 5.7: Half-cell potential difference data of Test Area 2

Axis	1	2	3	4	5	6	7	8	9	10
1	-310	-324	-496	-369	-469	-348	-220			-126
	-233	-100	-359	-273	-415	-280	-314	-390	-383	-526
	-303	-184	-289	-171	-422	-152	-189	-225	-201	-170
Average	-282	-203	-381	-271	-435	-260	-241	-308	-292	-274
2	-420	-319	-328	-368	-393	-344	-215	-235		
	-290	-224	-206	-249	-294	-277	-291	-506	-308	-387
	-432	-215	-150	-162	-191	-145	-165	-350	-162	-215
	-381	-253	-228	-260	-293	-255	-224	-364	-235	-301
3	-303	-316	-437	-374	-535	-349	-248			-160
	-208	-214	-456	-268	-658	-276	-325	-306	-281	-322
	-334	-180	-496	-193	-605	-167	-199	-187	-154	-136
Average	-282	-237	-463	-278	-599	-264	-257	-247	-218	-206
4	-307	-315	-352	-701	-367	-331	-208		-100	-183
	-326	-214	-262	-647	-273	-260	-277	-280	-275	-305
	-488	-192	-279	-601	-173	-145	-158	-169	-141	-124
	-374	-240	-298	-650	-271	-245	-214	-225	-172	-204
5	-298	-320	-328	-345	-377	-100	-130	-163	-190	
	-130	-200	-204	-237	-299	-284	-353	-322	-287	-308
	-237	-146	-135	-145	-199	-166	-252	-248	-150	-105
Average	-222	-222	-222	-242	-292	-183	-245	-244	-209	-207

Table 5.8: Average Half-cell potential difference data of Test Area 2

Axis	1	2	3	4	5	6	7	8	9	10
1	-282	-203	-381	-271	-435	-260	-241	-308	-292	-274
2	-381	-253	-228	-260	-293	-255	-224	-364	-235	-301
3	-282	-237	-463	-278	-599	-264	-257	-247	-218	-206
4	-374	-240	-298	-650	-271	-245	-214	-225	-172	-204
5	-222	-222	-222	-242	-292	-183	-245	-244	-209	-207

Table 5.9: Chance of rebar corrosion in Test Area 2

(Interpretation of results per ASTM C876)

Axis	1	2	3	4	5	6	7	8	9	10
1	50%	50%	95%	50%	95%	50%	50%	50%	50%	50%
2	95%	50%	50%	50%	50%	50%	50%	95%	50%	50%
3	50%	50%	95%	50%	VEC	50%	50%	50%	50%	50%
4	95%	50%	50%	VEC	50%	50%	50%	50%	5%	50%
5	50%	50%	50%	50%	50%	5%	50%	50%	50%	50%

VEC= Visible evidence of corrosion

CHAPTER 6: SUMMARY AND CONCLUSIONS

6.1 Research Objectives and Methods

The goal of this study was to assess the effectiveness of multiple nondestructive evaluation (NDE) methods to evaluate the condition of reinforced and prestressed concrete bridges exhibiting deterioration associated with corrosion of the steel reinforcement. The research plan was designed around an experimental approach and included both laboratory and field investigations. The objectives were to:

- Develop laboratory references, for selected NDE methods, for detecting and quantifying defects associated with corrosion of steel reinforcement and grout defects in post-tensioning applications.
- Evaluate the effectiveness of the selected NDE methods to detect and quantify deterioration in the field using both in service and decommissioned bridges.

The primary study effort focused on methods employed for evaluating deterioration of steel reinforcement including both prestressing strands and reinforcement. Side-by-side box beam bridges were selected for evaluation of the condition of prestressing strands and web reinforcement. Decommissioned box beams were tested in the laboratory to relate the impact of the estimated material deterioration, by the NDE methods, and the measured residual flexural capacity of the beams. Also a segmental bridge was included for evaluation of the condition of the web reinforcement and post-tensioning ducts. Specialized laboratory specimens were designed for this study to simulate debonding/voids around steel reinforcement, loss of cross section area of steel reinforcement, and various grouting challenges.

The principal NDE methods used were ultrasonic, magnetic and electrochemical. The following specific methods were used:

- Ultrasonic assessment for delamination, void detection and thickness measurements.
- Electro-chemical half-cell potential assessment for assessing the corrosive environment.
- Magnetic flux leakage assessment to estimate loss of cross sectional area of steel reinforcement and strands.

Ultrasonic testing was performed with MIRA 3D ultrasonic echo-pulse tomography using shear waves low-frequency phased antenna arrays. The corrosion potential (half-cell) measurements were completed using a copper-copper sulfate, reference electrode. The equipment used is known as CANIN. The magnetic flux leakage measurements were performed using a strong earth magnet mounted on a mobile unit. The change in magnetic field leakage as the magnet passes over the steel reinforcement, Hall Effect, was measured using Hall-Voltage sensors. The pilot version of the MFL mobile system was developed at the Center for Innovative Research, at Lawrence Technological University.

Supporting NDE methods were also employed and included:

- Impact hammer to detect surface variations, potential delamination and estimating in-situ concrete compressive strength.
- Cover meter to determine the location of steel reinforcement and concrete cover depth.
- Ground penetrating radar to determine the location of steel reinforcement (Operated by MDOT personnel during field investigations).

The summary of the application of the different methods is listed in Table 6.1. The list of laboratory specimens and field projects used is summarized in Table 6.2. A brief description of each laboratory specimen and its application in the project is summarized in Table 6.3. Similarly, a brief description of each field project and its application in this project is summarized in Table 6.4. The findings and discussion concerning selected box beams from the US-24 Middle Rouge River crossing are presented in Appendix B

Table 6.1: Summary of Research Methods used to Detect and Quantify Defects

Component	**Deterioration Type**	**NDE Methods to Detect**		**NDE methods to Quantify**	
		Laboratory	**Field**	**Laboratory**	**Field**
Reinforcement	Delamination & Voids Corrosion Activity	Ultrasonic -	Ultrasonic Half-cell	Ultrasonic -	Ultrasonic
	Loss of X-section Area	MFL	MFL	MFL	MFL Destructive*
PT Ducts	Voids & Grout Imperfections	Ultrasonic	Ultrasonic	Ultrasonic	Ultrasonic

*Laboratory destructive testing for verification

Table 6.2: Summary of Laboratory Specimens and Projects

Component	**Deterioration Type**	**Laboratory**	**Field**
Reinforcement	Delamination & Voids	Specimen 1 (2)**	Kent County; US-131; I-96
	Corrosion Activity	-	Kent County; US-131; I-96
	Loss of X-section Area	Specimen 2 (3)	Kent County
PT Ducts	Voids & Grout Imperfections	Specimen 3 (4)	US-131

** (#) indicates the number of samples in the specimen group

Table 6.3: Description of Laboratory Specimens

Identification	**Type**	**Description**
Specimen 1 S1-1 & S1-2 (Figure 3.7)	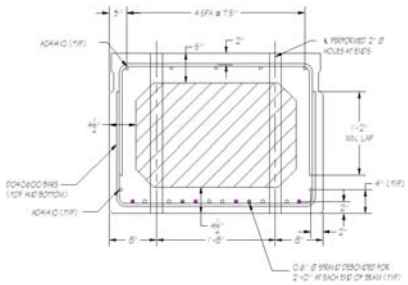	A range of defect types was introduced during construction such as delamination around reinforcement of varying lengths, grease on strands, shifts in interior cell, and honeycombs.
Specimen 2 S2-1, S2-2 & S2-3 (Figures 3.44 – 3.52)	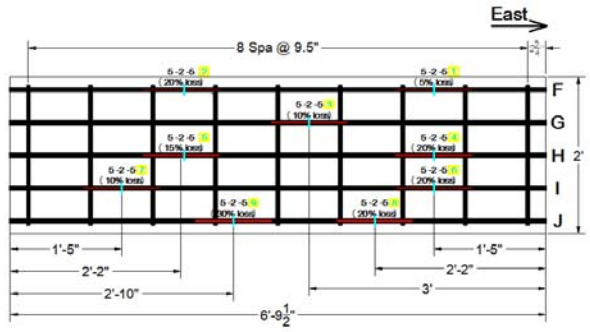	Loss of cross section area of steel reinforcement was simulated. S2-1 and S2-2 simulated single and double layer of rebar reinforcement. S2-3 simulated single layer of prestressing strands.
Specimen 3 S3-1 & S3-2 (Figures 3.62 & 3.63) S3-3 & S3-4 (Figure 3.64 & 3.65)	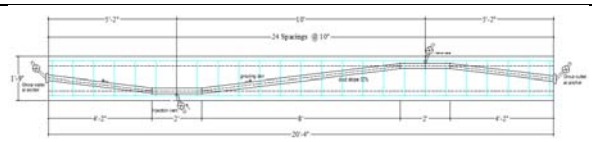 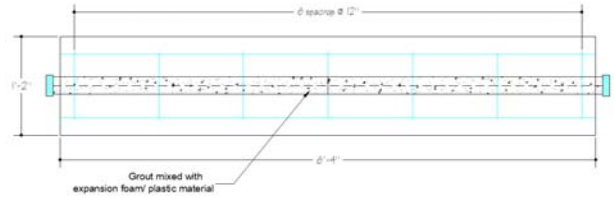	S3-1 and S3-2 are identical. Polyethylene corrugated draped ducts were used. The duct in S3-2 was partially filled with water prior to grouting to evaluate the ability to displace the water during the grouting process. S3-3 used steel duct and the grout was mixed with expansion foam and plastic material. S3-4 was grouted vertically.

Table 6.4: Description of Field Projects

Identification	Overview	Description
Kent County Side-by-side box beams J11, H6 and A1 Figure 3.83 & Fig. 3.90 -3.102		Relate the estimated deterioration with the residual flexural capacity of the box beams. Assess the extent of cross-sectional area loss due to corrosion of the bottom strands using magnetic flux leakage method (early stage, lab). Assess un-exposed sections of the beams for initiation of delamination around strands using the 3D ultrasonic tomography method. Assess chance of corrosion by half-cell measurements.
I-96 Side-by-side box beams (EB, Web on South face) Fig 3.120-3.124		Assess un-exposed sections of the beams for initiation of delamination around stirrups using the 3D ultrasonic tomography method. Assess chance of corrosion by half-cell measurements.
I-131 Segmental bridge Southbound Fig 3.103-3.119	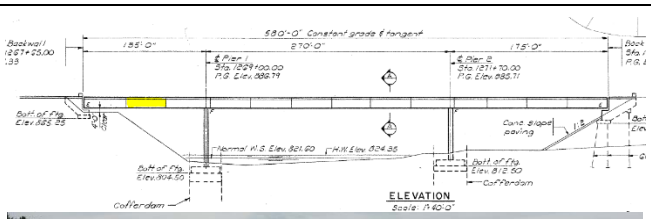 	Assess un-exposed sections of the beams for initiation of delamination around rebars in the web using the 3D ultrasonic tomography method. Assess chance of corrosion by half-cell measurements. Field pilot testing of magnetic flux leakage method. Assess grouting conditions in post-tensioning ducts.

6.2 Assessment of Defects Associated with Corrosion of Embedded Steel

In summary, ultrasonic echo-pulse tomography was able to detect debonding of the steel reinforcement and to detect internal voids and delamination. The method was able to quantify the depth of the defect but not the length of the defect. The MFL pilot demonstration showed that MFL can detect changes in the area of the steel reinforcement in laboratory and field applications.

6.2.1 Ultrasonic Testing

Ultrasonic assessment can detect typical deterioration of concrete such as debonding, delamination, and cracking that follows the corrosion process. Therefore, ultrasonic assessment can be employed as an indirect tool to detect corrosion of strands and reinforcement embedded in concrete. In advanced cases of corrosion, as observed in some of the field projects, with extensive delamination and cracking around strands and reinforcement, ultrasonic reflections near the corroded strands and reinforcement tend to produce voluminous surface noise and other multiple reflections. These reflections tend to mirror the actual reflections near the strands and any back-wall reflection from features such as the interior cell in a box beam. The ultrasonic pulse-echo data coalesces the responses from forty individual transducers that act as both transmitters and receivers. The transducers are arranged in an array with 4 rows and 10 columns covering a 4 in by 16 in (100mm by 400mm) surface area.

6.2.1.1 Laboratory Investigation

Based on the results from the comprehensive laboratory investigation on box beam specimens S1-1 and S1-2, it was determined that the ultrasonic echo-pulse tomography system could detect and locate the position of defects and voids around steel reinforcement. This was concluded from the evaluation that included locating the position of steel reinforcement and defects, and concrete thicknesses. The thickness of the bottom and top flanges as well as the web thickness were captured with 95% certainty at scanning frequencies of 50 – 100 kHz. The thicknesses were 125 to 150 mm (5 to 6 inches). However, due to the fact that higher frequencies have higher degree of attenuation, scanning frequencies should be limited to 50 to 70 kHz. There were some differences between the actual and diagnostic depth of the steel reinforcement when considering a 95% confidence interval. However, based on the localized scans on #4 (12.7 mm) reinforcement and 0.6” (15.24) mm

strands the ultrasonic echo-pulse method was able to locate the position of any steel reinforcement within ± 0.19 inch (4.9 mm) when the cover was about 2 inches (50 mm). Similarly, there were some differences between actual and diagnostic depth to the defects introduced around the embedded steel. The absolute depth of the defects (debonding between steel reinforcement and concrete) was detected within ± 0.14 inch (3.5mm) for a defect located at a depth of 1.77 inch (45 mm). Recall that the defects introduced debonding of the entire circumference of the steel reinforcement in lengths of 2, 4, 6 and 8 inches (50, 100, 150 and 200 mm).

6.2.1.2 Field Investigation

Ultrasonic testing should be carried out over large areas of the structure's surface to aid in detecting deviations from normal reflections. A comparative study of the laboratory ultrasonic assessments showed that the intensity of reflections were always higher in areas with defects around the steel reinforcement than in areas without defects. The assessment over large areas of the structure will therefore serve as a self-calibration since factors related to operator, materials, and construction can be assumed to impact the measurements equally. The scanning of large areas on the bottom of the Kent County box beams documented increased ultrasonic reflections near the strands in areas where visual inspection did not detect any deterioration. Furthermore, the analysis showed that scanning frequencies of about 50 to 70 kHz yielded the most consistent results. Application of higher frequencies should be avoided when assessing near surface features or thin structures such as box beam web or flanges.

In the US-131 segmental bridge, the ultrasonic testing on the web near one of the abutments showed poor concrete consolidation as well as diagonal cracking. This area showed significantly higher reflection intensities compared to another web area in a mid-span region. The analysis of the area near the support was complicated by the fact that the cracks were sealed and the sealing material was smoothed at least 25 mm (1 inch) on each side of the crack. It is unclear how much impact this intermittent surface coating had on the overall results.

6.2.2 Half-Cell Potential Differences

6.2.2.1 Field Investigation

The half-cell measurements were analyzed using contour, frequency plots in addition to the absolute values. The contour plots quickly identifies regions with significant change in potentials and the frequency plots quickly illustrates the relative area with high, medium and low chance of corrosion. Note that in the three (3) decommissioned box beams from Kent County an electrical circuit was established with connection to the prestressing strands, and in the US-131 and I-96 projects the circuits were closed with the web reinforcement.

The assessment of the Kent County box beam bottom surfaces illustrated that the shear key regions and the fascia surfaces typically exhibited increased chance of corrosion compared to the rest of the bottom flange. The exterior beams were identified as having the largest active corrosion regions with more than 20% and 60 %, respectively, of the bottom surface having 50 % or higher chance of corrosion. In contrast, the interior beam showed less than 10% of the bottom surface had 50 % chance of corrosion.

The concrete in the interior web in the US-131 segmental bridge was poorly consolidated and there were honeycombs and significant voids visible to the naked eye. Because the concrete surface is to be wetted uniformly prior to taking half-cell potential measurements, it is unknown if the highly porous concrete surface caused the half-cell potential differences to be higher than on a similar well consolidated concrete. The readings indicated a highly corrosive environment that under normal circumstances would have been associated with visible signs of corrosion in discrete areas. Visible signs of corrosion were not observed. It is assumed that the high humidity environment caused by the river increased the humidity in the concrete uniformly. Therefore, the river environment did not cause the difference in half-cell potential readings between the two different web areas.

Measurements of half-cell potential differences between the surface of the concrete and the reinforcement is an excellent tool to use in combination with the ultrasonic testing to confirm localize areas with corrosion activities. This study found excellent agreement between the two methods. When the half-cell potential difference increased severity level, it was typically associated with increased ultrasonic reflections near the steel reinforcement in that same area. This was evident for the bottom surfaces of the Kent County box beams and the web of the exterior beam on the I-96 project, where both structures did also show regions of visible evidence of corrosion such as surface rust stains and cracks. In the I-96 structure, the concrete cover had spalled from the web reinforcement near the support. It appeared as the concrete cover was inadequate as the exposed stirrups were found at about 1/2 inch (12.5 mm) from the web surface. The overall web thickness was estimated by ultrasonic measurements to be 6 inches (150 mm) as designed.

Considering the combined results of the electrochemical and ultrasonic testing of the US-131 segmental bridge, it is clear that the poor consolidation resulted in internal voids as well as those observed on the surfaces. Furthermore, the concrete is in an environment that is very conducive to corrosion despite no visible signs of corrosion at the time of testing.

6.2.2.2 Quantify Defects Associated with Corrosion of Embedded Steel

The findings and conclusions presented in Section 6.2.1 showed that results from ultrasonic echo-pulse tomography testing can detect the simulated gap created around a reinforcement or strand as part of the steel corrosion process. Furthermore, the analysis of the results from the Kent County box beams showed that the intensity of the reflections are much increased when delamination has developed. Therefore, ultrasonic testing can clearly capture the difference in the level of severity. However, other methods are needed to quantify the extent of corrosion and more specifically quantify the loss of reinforcement material.

The decommissioned box beams made available for this study allowed correlations to be made between the measured flexural capacity and the predicted capacity calculated considering the estimated material deterioration based on NDE results. The loss of cross section area of the flexural reinforcement was estimated based on magnetic flux leakage (MFL) measurements. The calibration of the MFL mobile scanner was based on laboratory investigations, preliminary assessment and initial field deployment was performed on the decommissioned box beams from Kent County at LTU and on the bottom flange of the US-131 project. The associated findings and conclusions from application of the MFL system is summarized below.

6.2.3 Magnetic Flux Leakage Measurements

The magnetic flux leakage method relies on a comparative method to assess the loss of steel cross sectional area. Laboratory developed calibration curves are based on the difference in Hall Voltage representing the magnetic flux leakages for steel reinforcement of different sizes. Then a comparative assessment between estimated and actual average loss of reinforcement area over a length of 3 inches and 12 inches (75 mm and 300 mm) was conducted, respectively. The influence of the location of shear reinforcement was also evaluated. In general, the method predicts the same rate of loss as measured. However, for the reinforced calibration beams the stirrup spacing and the length of the defect did influence the results. In general, very good agreement was obtained between predicted and actual loss for stirrup spacing of 9.5 inches (241 mm) whereas the predicted loss was overestimated at a constant absolute value of +10% of the cross section area when the stirrup spacing was 19.5 inches (495 mm). Further, post processing of the data is needed to refine the analysis to consider the effect of the distance between the defect and the stirrups. However, the development of an automated procedure is not within the scope of this study. The majority of the field applications in this study contained #4 (12.7 mm) and #5 (15.24 mm) reinforcement and 0.5 inch or 0.6 inch diameter prestressing strands with a concrete cover of 1.5 inch (37 mm).

The first test field deployment of the mobile MFL scanner was to assess any challenges associated with testing, data collection, and analysis of results. The scanner was deployed on the US-131 project and the bottom flange was selected as a test area. The test area was approximately 169 inches (4300 mm) long and 118 inches (3000 mm) wide reinforced with a 10 inches by

7 inches (250 mm by 175 mm) steel reinforcement mat. One issue encountered was the unfinished, rough surface of the bottom flange. The MFL mobile scanner has a clearance of ¾ inch which was not enough for an uneven surface. This was not an issue with previous testing of laboratory prepared and the Kent County beams since those beams had smooth surfaces. This issue was resolved by using 1/8" wood strips drive tracks for the MFL mobile scanner. Another issue encountered was that the permanent magnets were collecting excess magnetic materials from the floor. Buildup of magnetic material influences the measurements, and for future applications on surfaces or decks it is necessary to have the test area swept using a magnetic sweeper before scanning.

The pilot deployment of the MFL system was performed on the US-24 box beam bridge over Middle Rouge River. The box beams were designed with two layers of flexural reinforcement with thirteen (13) 3/8" prestressing strands in each layer. Two box beams were assessed. The MFL scanner was traversing up-side-down along the strnds and was carried by the research assistants. The primary challenge is to maintain full contact between the mobile scanner and the concrete surface as well as making sure that the scanner does not wander from the strand position. One box beam exhibited severe signs of concrete surface deterioration and corrosion stains along both shear keys with the deterioration worsening towards the abutment. The other box beam exhibited some visual deterioration near the shared shear key with the first beam. The MFL assessment indicates, for the severely corroded beam, that three of the thirteen strands were broken, five strands were corroded at varying levels resulting in cross section loses ranging from 15 to 75 %, the remaining five strands were in good condition. The strands in the second box closest to the shared shear key exhibited minor variations in the magnetic flux leakage. The rest of this second beam did not indicate corrosion.

6.2.4 Destructive Testing

The flexural capacity of the three (3) Kent County decommissioned box beams was determined at the Center for Innovative Material Research at Lawrence Technological University. The measured ultimate capacity was in good agreement with the estimated ultimate capacity considering the

estimated loss of flexural reinforcement due to corrosion. The concrete compressive strength of 6,100 psi (42 MPa) was estimated from results obtained with an impact hammer. The estimated loss of reinforcement was based on the results from the early stage development of the MFL system and visual observations (e.g. broken strands). The residual flexural capacity of the box beam assuming 2 broken strands at the exterior edge and 20 % loss of remaining strands was about 62 % compared to the estimated 58% calculated prior to testing. Since the overall condition was similar for the remaining two beams it was estimated that the average strand cross sectional area loss was 10 %. The residual capacity was measured to be 73 % and 79 %, respectively, compared to the calculated 89 % prior to testing. It should be noted that both of these box beams experienced the majority of the corrosion related deterioration at one of the shear keys. This caused that side of the beam to fail first rotating the beams during the final failure stages. It is likely that this instability, in part, caused the additional reduction in capacity.

6.3 Assessment of Grouting Defects in Post-tensioning Ducts

6.3.1 Laboratory Simulations

Common grouting problems recognized in the field are insufficient grout coverage at angle breaks (change from positive to negative moment regions), incomplete displacement of standing water in the ducts prior to grouting, and imperfections in the grouting material. The ultrasonic echo-pulse testing, on laboratory post-tensioned specimens, showed clearly the location of the empty ducts when either polyethylene corrugated or steel corrugated duct material was used. Furthermore, ultrasonic testing after grouting showed a significant reduction in reflections from the duct area irrespective of duct material used.

The laboratory simulated grouting operation for the draped duct configuration showed that full grout coverage was achieved at the angle breaks and that the water was fully displaced from the duct, through the vent, as the grout material was pumped in. This was confirmed using a comparative assessment of the intensity of the ultrasonic reflection along the length of the ducts. On the other hand the ultrasonic testing was not able to detect changes in the intensity of reflection from the duct when the grout had been mixed with polystyrene (defects).

6.3.2 Field Explorations

The segmental bridge from the US-131 project was constructed with transverse post-tensioning in the top flange and longitudinal post-tensioning in the bottom flange. Both types of ducts were assessed on the interior side of the segmental bridge hence limiting the assessment of the transverse post-tensioning ducts to the center length and not including the anchor area in the overhang. The assessed longitudinal ducts was located between two piers.

The ultrasonic testing of the concrete surface above the location of a longitudinal post-tensioned duct clearly showed the location of the duct and the bottom of the flange as indicated by the increased intensity of the reflections. At the same time, the intensity of the reflections from the ducts appeared unchanged along the entire length of the duct suggesting no change in grout or that the duct material have significantly different density compared to that of concrete. When the 3D tomography plots from the field application are compared to those from the laboratory simulation it is noted that the intensity of the reflections in the field application are higher for the same testing frequency of 50 kHz. Ultrasonic assessment on the anchor blocks did reveal increased reflections from areas around the duct. These reflections are suspected to be caused by the reinforcement cages in a congested area.

Visible transverse cracks were observed on the concrete road surface at the same spacing as the transverse ducts. These cracks, however, had at the time of testing not propagated through the thickness of the top flange as they were not seen inside the segmental bridge. The research team did not have access to the road. Ultrasonic assessment along the length of transverse post-tensioned ducts showed similar reflected intensities with no significant differences. Therefore, it is assumed that the ducts are fully grouted. On the other hand, it was noted that the intensity of the reflections from the transverse duct tended to be higher than that of the longitudinal ducts. It is possible that the transverse cracks observed on the road surface coalesced with the ducts and caused the increased reflection.